Please cite this article in press as: De Santis et al., *FUS* Mutant Human Motoneurons Display Altered Transcriptome and microRNA Pathways with Implications for ALS Pathogenesis, Stem Cell Reports (2017), https://doi.org/10.1016/j.stemcr.2017.09.004

Stem Cell Reports
Article

OPEN ACCESS

FUS Mutant Human Motoneurons Display Altered Transcriptome and microRNA Pathways with Implications for ALS Pathogenesis

Riccardo De Santis,[1,2] Laura Santini,[2] Alessio Colantoni,[2] Giovanna Peruzzi,[1] Valeria de Turris,[1] Vincenzo Alfano,[2] Irene Bozzoni,[1,2,3] and Alessandro Rosa[1,2,*]
[1]Center for Life Nano Science, Istituto Italiano di Tecnologia, Viale Regina Elena 291, 00161 Rome, Italy
[2]Department of Biology and Biotechnology Charles Darwin, Sapienza University of Rome, P.le A. Moro 5, 00185 Rome, Italy
[3]Institute Pasteur Fondazione Cenci-Bolognetti, Sapienza University of Rome, P.le A. Moro 5, 00185 Rome, Italy
*Correspondence: alessandro.rosa@uniroma1.it
https://doi.org/10.1016/j.stemcr.2017.09.004

SUMMARY

The *FUS* gene has been linked to amyotrophic lateral sclerosis (ALS). FUS is a ubiquitous RNA-binding protein, and the mechanisms leading to selective motoneuron loss downstream of ALS-linked mutations are largely unknown. We report the transcriptome analysis of human purified motoneurons, obtained from *FUS* wild-type or mutant isogenic induced pluripotent stem cells (iPSCs). Gene ontology analysis of differentially expressed genes identified significant enrichment of pathways previously associated to sporadic ALS and other neurological diseases. Several microRNAs (miRNAs) were also deregulated in *FUS* mutant motoneurons, including miR-375, involved in motoneuron survival. We report that relevant targets of miR-375, including the neural RNA-binding protein ELAVL4 and apoptotic factors, are aberrantly increased in *FUS* mutant motoneurons. Characterization of transcriptome changes in the cell type primarily affected by the disease contributes to the definition of the pathogenic mechanisms of *FUS*-linked ALS.

INTRODUCTION

The fatal neurodegenerative disease amyotrophic lateral sclerosis (ALS) is caused by loss of motoneurons (MNs) in the spinal cord and brain, leading to progressive muscle atrophy. Both sporadic ALS (sALS) and familial ALS (fALS) have been linked to a number of genes, including *SOD1*, *C9ORF72*, *TDP-43*, *TAF15*, and *FUS/TLS* (*FUS*) (Renton et al., 2014). The *FUS* gene encodes for an RNA-binding protein involved in RNA biogenesis and maturation (Lagier-Tourenne et al., 2012). Wild-type (WT) FUS is mainly localized in the nucleus, and a hallmark of *FUS* ALS patients is the presence of cytoplasmic inclusions containing mutated protein in the brain and spinal cord (Kwiatkowski et al., 2009; Vance et al., 2009). Many ALS-associated *FUS* mutations disrupt the function of the C-terminal nuclear localization signal (NLS). Therefore, defects in nuclear import, leading to aberrant cytoplasmic localization of FUS, have been proposed as the initial step in ALS pathogenesis (Bentmann et al., 2013; Dormann and Haass, 2011). Recent analyses in murine models suggest that loss of FUS function may not be sufficient to induce MN degeneration (Kino et al., 2015; Scekic-Zahirovic et al., 2016), and both loss of a nuclear function and gain of a toxic function in the cytoplasm have been proposed as contributing pathological mechanisms in *FUS* ALS (Ling et al., 2013).

FUS mutations are expected to exert a major change in the transcriptome. However, this has not been directly addressed in human MNs so far. Human induced pluripotent stem cells (iPSCs) represent a useful system to model ALS, as they can be differentiated into disease-relevant cell types (Sances et al., 2016). iPSCs carrying ALS mutations can be generated by reprogramming from patients (Boulting et al., 2011) or by gene-editing techniques, producing lines that differ only for the specific mutation (Kiskinis et al., 2014; Lenzi et al., 2015). Comparison of gene-edited mutant lines with their otherwise isogenic WT counterparts allows to assign any observed phenotypic difference to the ALS mutation, avoiding any bias due to different genetic backgrounds of non-isogenic mutants and controls.

Recent evidence suggests that microRNAs (miRNAs) might play a role in MN diseases, such as ALS and spinal muscular atrophy (SMA) (Kye and Gonçalves, 2014). Conditional loss of the processing enzyme Dicer in postnatal MNs causes an SMA-like phenotype in mice (Haramati et al., 2010), suggesting that, collectively, miRNAs could be required for MN survival. Global downregulation of miRNAs was observed in MNs of sporadic ALS spinal cords isolated by laser-capture microdissection (Emde et al., 2015), and a protective role for individual miRNAs, such as miR-218 and miR-375, has been shown in MNs (Amin et al., 2015; Bhinge et al., 2016). Previous work from our lab and others has shown that proteins genetically linked to ALS play a role in miRNA biogenesis. FUS stimulates miRNA processing by facilitating the recruitment of the enzyme Drosha on miRNA genes (Morlando et al., 2012), and TDP-43 regulates miRNA biogenesis at multiple levels (Buratti et al., 2010; Di Carlo et al., 2013; Kawahara and Mieda-Sato, 2012). Moreover, overexpression of SOD1, TDP-43, or FUS proteins, either WT or carrying ALS mutations, impaired miRNA processing in the cytoplasm by inducing cellular stress (Emde et al., 2015). As most of the studies on the contribution of ALS-linked factors to miRNA biogenesis come from cell lines or non-MN cells, it is currently unknown which miRNAs could be affected by ALS mutations in MNs.

Here we took advantage of mutant FUS^{P525L} and isogenic control iPSCs to generate and isolate pure human MNs, which were used for whole-transcriptome analysis by RNA sequencing (RNA-seq). We identified both long and short RNA species significantly altered in *FUS* mutant MNs. Changes in the transcriptome point to pathways previously associated to neurodegenerative diseases, such as those related to cell adhesion. Among differentially expressed miRNAs we focused on miR-375. Levels of miR-375 were decreased in mutant MNs, in which we observed an increase of a subset of its targets, such as p53 and the neural RNA-binding protein ELAVL4. We propose a pathological mechanism in which an impairment of miRNAs production, downstream of *FUS* mutations, would alter RNA metabolism and increase MN vulnerability via aberrant upregulation of pro-apoptotic targets.

RESULTS

Differentiation and Isolation of iPSC-Derived MNs

We have recently reported the generation of iPSC lines devoid of mutations in the *FUS* gene (hereafter FUS^{WT}) or carrying the severe P525L ALS-related mutation introduced by gene editing in both *FUS* alleles (hereafter FUS^{P525L}) (Lenzi et al., 2015). We stably modified these lines by inserting a *Hb9*:GFP reporter into the *AAVS1* locus (Wainger et al., 2014) (Figures S1A and S1B). To improve time and efficiency of MN generation from iPSCs, we took advantage of an optimized protocol based on neural induction and patterning of differentiating cells in adhesion conditions (Figure 1A). Using this protocol we consistently obtained MN progenitors in a 12 day time frame. A time course analysis of marker expression in differentiating FUS^{WT} cells is shown in Figure 1B. By day 6, cells lose the pluripotency marker *NANOG*. Around this time point we detected a peak of expression for the neural progenitor gene *PAX6*, followed by a raise of pan-neuronal (*TUJ1*) and MN (*ISL1*) markers at day 9. The late MN gene *CHAT* was expressed at day 9, with a further increase until day 12. Levels of the MN progenitor marker *HB9* peaked around day 9 and decreased at later time points. The mixed population of differentiated cells at day 12 was highly enriched of *ISL1/2*-positive neurons (Figure S1C). Live cell imaging and flow cytometry analysis indicated that 30%–40% of cells were GFP-positive at this time point (Figures 1C and 1D). Notably, expression of the reporter was detected only in retinoic acid and smoothened agonist (SAG)-treated cells, which induce a ventral spinal cord character, suggesting that the exogenous *Hb9* promoter was correctly turned on in the MN lineage (Figure 1E). We further validated the reporter system by gene expression analysis in distinct cell populations isolated using cell sorting (Figure S1D). Next-generation sequencing (RNA-seq) was performed on total RNA from GFP-positive and -negative cells collected after sorting. Cluster analysis based on gene expression data correctly separated the samples into GFP-positive and -negative ones (Figures S1E and S1F). GFP-positive samples had a similar expression profile, while GFP-negative ones were more dissimilar. A total of 1,631 genes were differentially expressed between GFP-positive and -negative cells, most of them having higher expression levels in GFP-negative samples (Figure S1G; Table S1). As shown in Figure 1F, levels of MN markers (in green) were higher in GFP-positive samples, with the exception of *LHX1*. Notably, the *HB9* transcript was not significantly enriched in GFP-positive samples. This apparent inconsistency can be explained by the narrow window of time of HB9 expression: by the time point in which GFP protein reaches its maximum accumulation (day 12; Figure 1D) the endogenous *HB9* mRNA is already downregulated (Figure 1B). Compared with GFP-positive cells, GFP-negative populations probably contained a fraction of MN progenitors at earlier stages, expressing high levels of *HB9*. As expected, ALS-related genes *SOD1*, *C9ORF72*, *FUS*, and *TARDBP* were not enriched in GFP-positive cells. Experimental validation of selected markers by real-time qPCR confirmed the RNA-seq results (Figure 1G). Purified GFP-positive cells were re-plated on laminin-coated dishes and upon further culturing acquired a neuronal morphology (Figure S1H). Immunostaining analysis indicated that sorted GFP-positive cells were highly enriched for *ISL1/2*-positive MNs (Figure 1H).

Taken together, the combination of a short and efficient differentiation protocol and the stable insertion of the *Hb9*:GFP reporter allowed the effective isolation of a large number of purified, iPSC-derived, MNs.

Transcriptome Profiling in FUS WT and Mutant Human MNs

We have previously shown that ALS mutations in *FUS* do not impair differentiation (Lenzi et al., 2015, 2016). This observation was confirmed in MNs generated with the improved protocol described in Figure 1 from FUS^{WT} and FUS^{P525L} iPSCs. The fraction of GFP-positive cells was consistently comparable over six independent experiments (Figures 2A and 2B). Moreover, GFP-positive cells with a FUS^{WT} or FUS^{P525L} background showed comparable levels of expression of MN markers (Figure S2A). Notably, in the *Hb9*:GFP FUS^{P525L} line both the mutation and the reporter system have been introduced by gene editing. Therefore, besides the FUS^{P525L} mutation, iPSC lines used for subsequent experiments were isogenic.

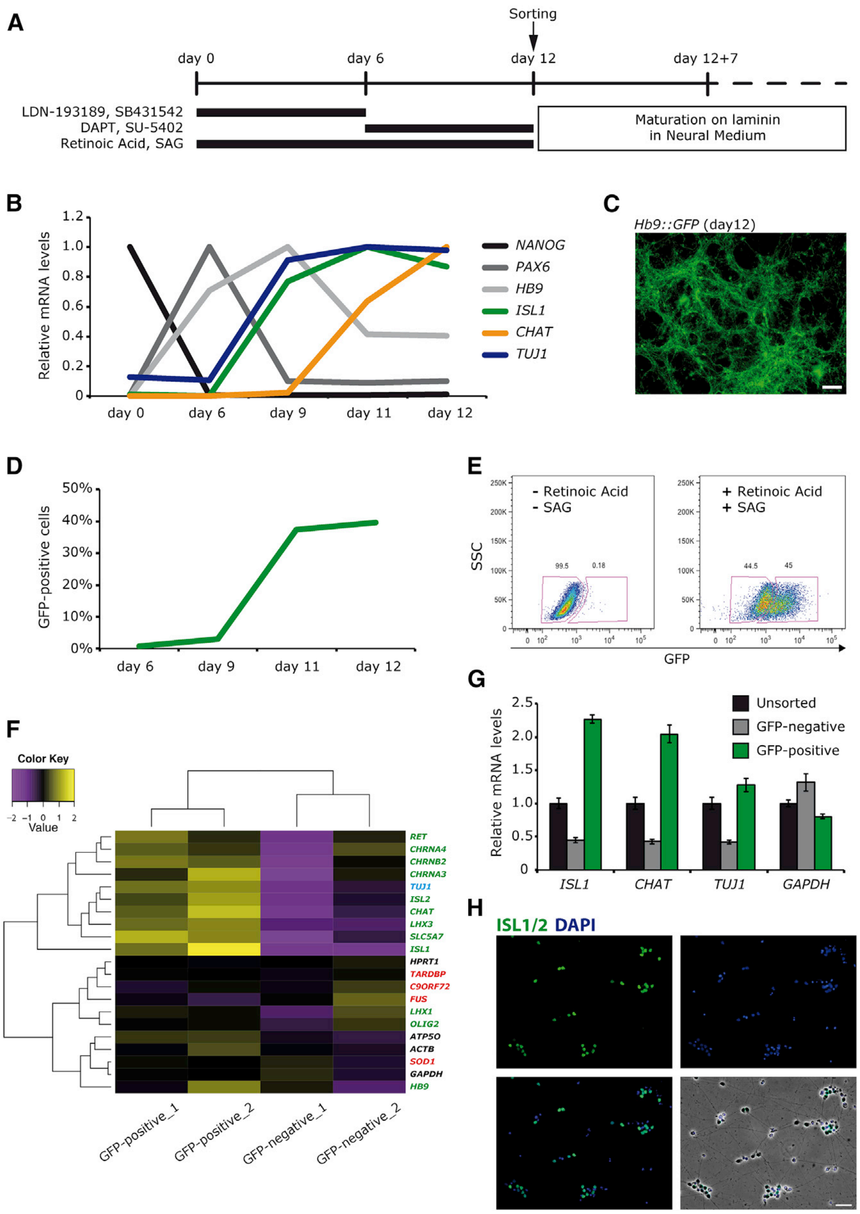

Figure 1. MN Differentiation Protocol and *Hb9*:GFP Reporter

(A) Schematic representation of the differentiation protocol.

(B) Real-time qRT-PCR marker expression analysis. For each marker the time point with the highest expression has been used as the calibrator sample.

(C) Live cell imaging of GFP expression in differentiated cells at day 12. Scale bar, 80 μm.

(D) Schematic representation of flow cytometry analysis of the fraction of GFP-positive cells during differentiation.

(E) Cells were differentiated as in (A) in the presence (right) or in the absence (left) of retinoic acid and SAG, and analyzed by fluorescence-activated cell sorting (FACS) at day 12.

(F) Heatmap representing expression levels of selected genes in sorted GFP-positive and -negative cells (two independent experiments). Plotted values correspond to mean-centered log2-transformed reads per kilobase of transcript per million mapped reads (RPKM) values. MN markers are indicated in green, ALS genes in red, and housekeeping controls in black.

(G) Real-time qRT-PCR analysis of the expression of the indicated genes in unsorted cells (black bars) and GFP-negative (gray bars) and GFP-positive (green bars) cells isolated by FACS (day 12). For each gene the unsorted cells sample has been used as calibrator. Histogram bars represent the average of a technical replicate (n = 3) and error bars indicate the SD.

(H) Immunostaining analysis of sorted MNs (day 12 + 3) with an anti-ISL1/2 antibody (green). Nuclei were stained with DAPI (blue). Upper panels show single channels. Lower panels show merged channels and overlay with the phase contrast image. Scale bar, 40 μm. See also Figure S1.

We took advantage of our iPSC system to systematically analyze the consequences of the FUS^{P525L} mutation on the transcriptome in pure populations of *in-vitro*-derived human MNs. GFP-positive FUS^{WT} and FUS^{P525L} iPSCs were sorted at day 12 of differentiation and further cultured on laminin-coated dishes for an additional 7 days (day 12 + 7). Total RNA from three independent differentiation experiments was collected and analyzed by RNA-seq. Gene expression-based cluster analysis resulted in the segregation of samples into two distinct groups based on their *FUS* genotype (Figures S2B and S2C). Out of 14,289 genes expressed in human MNs, 267 genes were upregulated and 244 downregulated in a consistent manner in FUS^{P525L} compared with FUS^{WT} (false discovery rate [FDR] < 0.05) (Table S1). The gene expression heatmap of differentially expressed genes is shown in Figure 2C. RNA-seq results were validated by real-time qPCR in at least three additional independent samples. Figure 2D shows validation of four representative genes among those downregulated (*SCL17A8*, *NXPH2*, *CRIM1*, and *GRIN2A*) and upregulated (*TP53I3*, *CDH7*, *NNAT*, and *TSPYL5*). Expression of the *FUS* transcript itself, as well as the mRNAs of other major

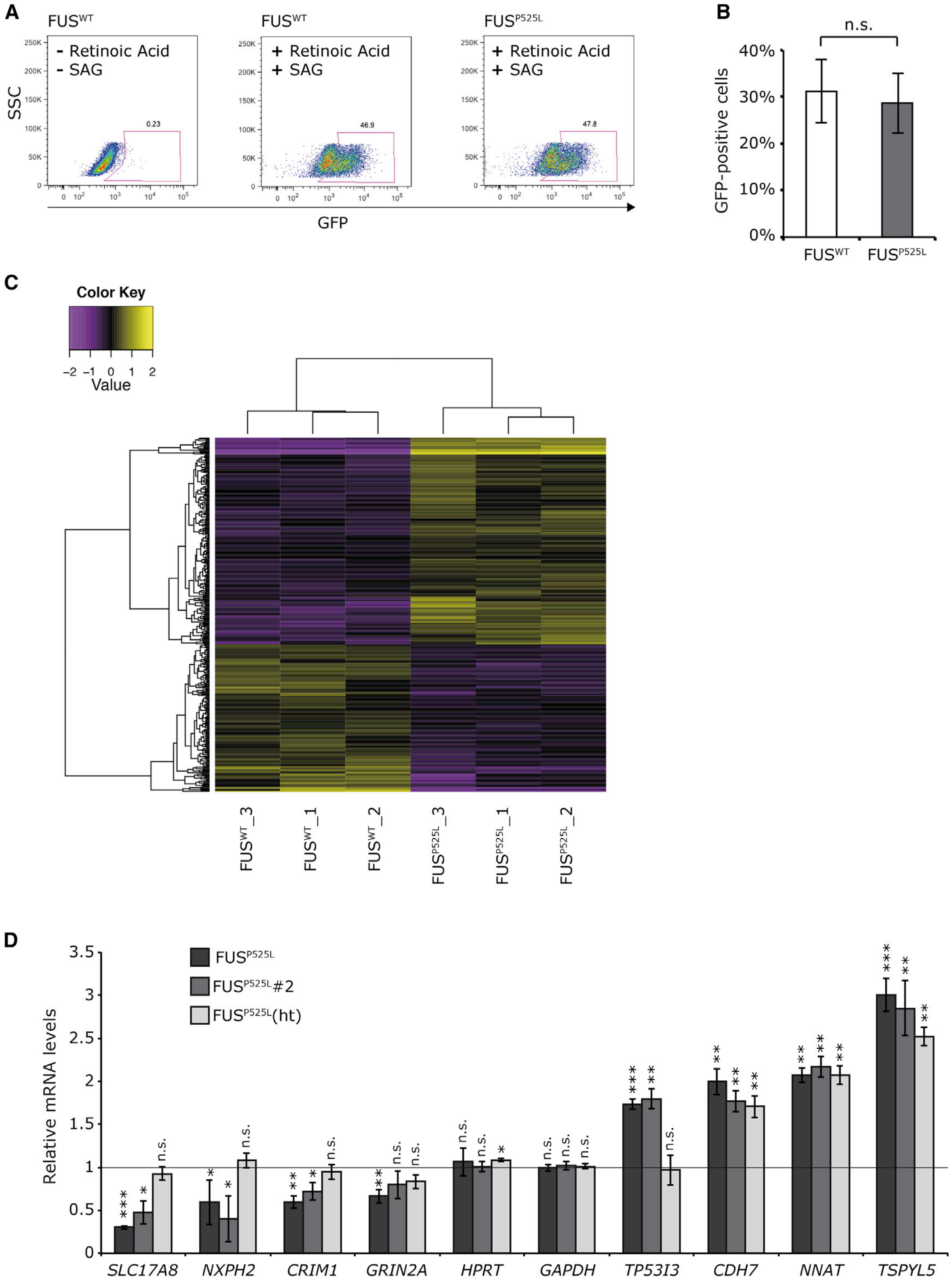

Figure 2. RNA-Seq Analysis of FUS^{WT} and FUS^{P525L} iPSC-Derived MNs

(A) Representative FACS plots of FUS^{WT} and FUS^{P525L} cells at day 12. As a negative control, FUS^{WT} cells were differentiated in the absence of retinoic acid and SAG (left panel).

(B) Schematic representation of flow cytometry analysis (day 12). Histogram bars represent the average of six independent experiments and error bars indicate the SD (Student's t test; unpaired; two tails; n.s., $p > 0.05$).

(legend continued on next page)

ALS-related genes, was not significantly altered in *FUS* mutant MNs (Figure S2D).

We confirmed these results in an independent *FUS* WT and mutant isogenic pair. A second FUS^{P525L} iPSC line (hereafter FUS^{P525L}#2), generated as previously described (Lenzi et al., 2015), and its parental FUS^{WT} iPSC line (hereafter FUS^{WT}#2) were modified by inserting the *Hb9*:GFP reporter into the *AAVS1* locus (Figures S3A–S3D). FUS^{WT}#2 and FUS^{P525L}#2 were then differentiated, sorted, and collected at day 12 + 7 for RNA analysis. All genes analyzed in the original isogenic pair resulted consistently altered in MNs obtained from these new iPSC lines (Figure 2D).

A subset of these genes was also affected in MNs obtained from a *Hb9*:GFP-modified heterozygous FUS^{P525L} iPSC line, hereafter FUS^{P525L}(ht) (Lenzi et al., 2015) (Figure 2D).

Functional Consequences of the FUS^{P525L} Mutation in Human MNs

We next assessed whether the change in the transcriptome detected in *FUS* mutant cells might be informative of pathways potentially involved in ALS MN degeneration. Gene ontology (GO) term enrichment analysis with the FIDEA tool (D'Andrea et al., 2013) highlighted relevant categories that cooperate in pathways and distinct molecular functions. In particular, we noticed a striking enrichment for categories related to cell adhesion in genes differentially expressed in FUS^{P525L} MNs (Figure 3A). Notably, "cell adhesion" is one of the categories consistently enriched in multiple studies focusing on FUS-bound transcripts and splice targets in mouse and human neurons (Orozco and Edbauer, 2013). GO term enrichment analysis of differentially expressed genes in laser-captured MNs from postmortem sporadic ALS patients also indicated "cell adhesion" (Batra et al., 2016). Moreover, functional enrichment analysis for genome-wide association studies involving several neurological diseases (including ALS) showed significant values for the "cell-cell adhesion" GO category (Guio-Vega and Forero, 2017). This category was also enriched in the analysis of differentially expressed genes in ALS fibroblasts carrying the *C9ORF72* mutation (Kotni et al., 2016). Cell adhesion-related categories were enriched also when upregulated and downregulated genes were analyzed separately (Figure S4A). Interestingly, the Kyoto Enrichment of Genes and Genomes pathway "Neuroactive ligand-receptor interaction" was specifically enriched by the downregulated genes. Previous work found this pathway enriched in RNA profiling from *C9ORF72* mutant fibroblasts (Kotni et al., 2016) and linked to neurological diseases such as Parkinson's disease (Kong et al., 2015).

Seeking for ALS signature in *FUS* mutant MNs, we crossed our RNA-seq data with a recently published dataset from laser-captured MNs fom sALS patients (Batra et al., 2016; Kapeli et al., 2016). In these works, the authors found 2,346 upregulated and 955 downregulated genes in sALS patients. The variation of upregulated genes was more robust, since more stringent selection criteria had lower impact on their abundance. These two lists of genes were employed as two distinct gene sets in the context of a gene set enrichment analysis to evaluate whether they were over-represented in the set of genes deregulated upon *FUS* mutation. Notably, the set of genes downregulated in sALS patients was enriched among those downregulated in FUS^{P525L} (FDR = 0.151), and the set of genes upregulated in sALS patients was significantly enriched among those upregulated in FUS^{P525L} (FDR = 0.009) (Figure S4B). These results suggest a common signature in gene expression between *in-vitro*-derived FUS^{P525L} MNs and sALS MNs. As suggested by FDR values, this tendency is stronger for the upregulated genes, consistent with the robustness of their deregulation in sALS patients.

We next investigated whether there is any relationship between differential gene expression and direct FUS binding in mutant MNs. The FUS interactome has never been characterized in purified human MNs; however, FUS CLIP-seq (crosslinking and immunoprecipitation, followed by high-throughput sequencing) data from human brain cortex are available (Lagier-Tourenne et al., 2012). We reanalyzed this dataset and evaluated the position of FUS binding clusters relative to the different regions of the pre-mRNAs, which are expressed in our MNs. FUS binding was enriched in the exonic regions of protein-coding genes, and in particular in the 3′ UTR, when compared with sequences located more (distal introns) or less (proximal introns) than 500 bp from the nearest exon-intron junction (Figure 3B). FUS-bound genes were classified as differentially expressed or not in FUS^{P525L} MNs, and individual mRNA regions were analyzed separately. A significantly higher percentage of genes modulated in FUS mutant MNs was directly bound by FUS in the distal intron and 3′ UTR (Figure 3C). When the same analysis was repeated with the TDP-43-bound genes dataset (Tollervey et al., 2011), we did not observe a significant enrichment

(C) Heatmap representing RNA-seq-derived expression levels of differentially expressed genes at day 12 + 7 (three independent experiments). Plotted values correspond to mean-centered log2-transformed RPKM values.

(D) Validation of selected genes by real-time qRT-PCR in MNs at day 12 + 7. Expression levels in FUS^{P525L}, FUS^{P525L}#2, and FUS^{P525L}(ht) are shown as relative to their respective isogenic FUS^{WT} controls, set to a value of 1. Histogram bars represent the average of at least three independent experiments and error bars indicate the SD (Student's t test; paired; two tails; $^{*}p < 0.05$; $^{**}p < 0.01$; $^{***}p < 0.001$; n.s., $p > 0.05$). See also Figures S2 and S3.

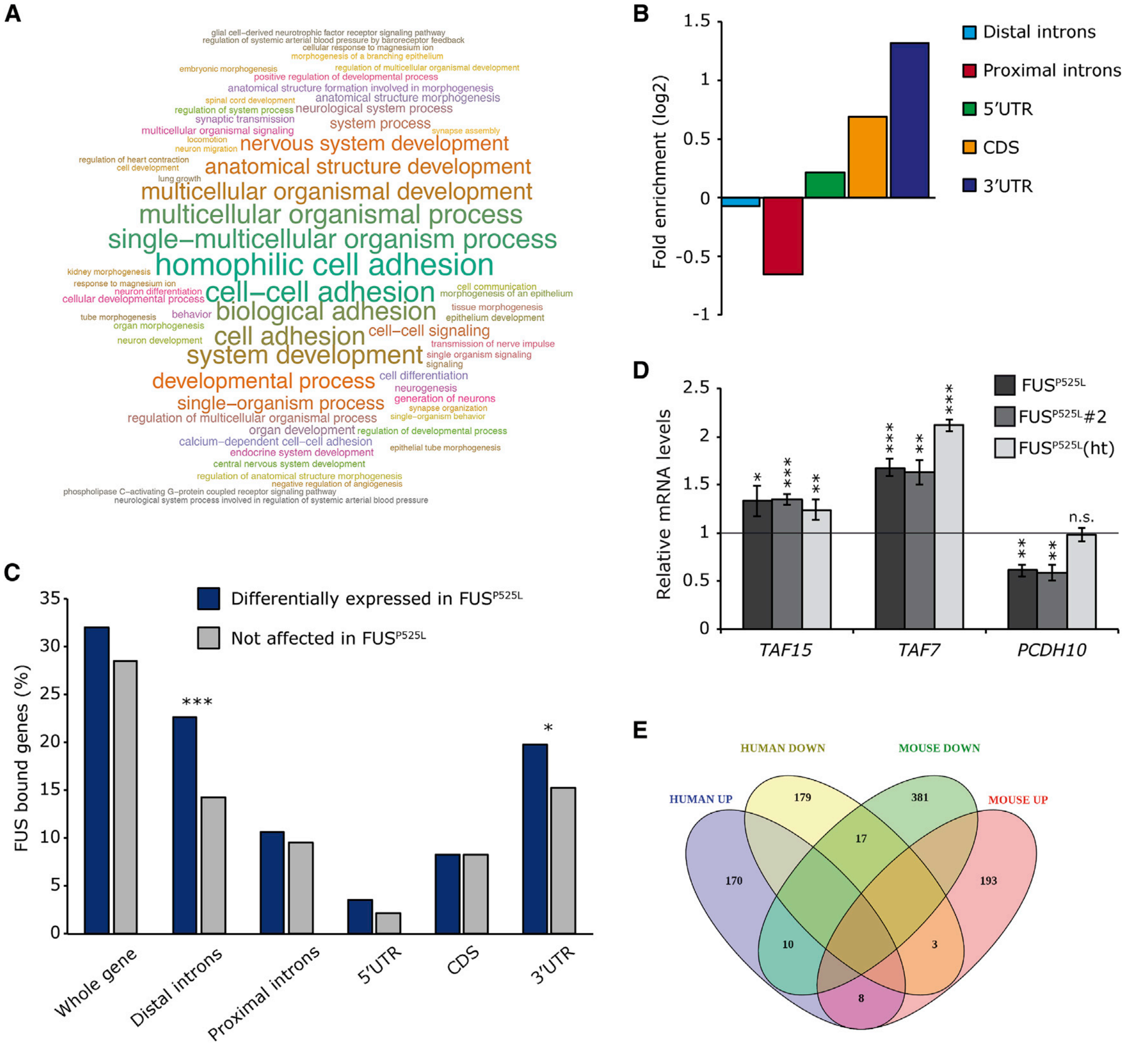

Figure 3. Bioinformatics Analysis of Differentially Expressed Genes in FUS^{WT} and FUS^{P525L} MNs

(A) Word cloud generated by FIDEA representing GO biological process terms enriched in the list of genes that are differentially expressed between FUS^{WT} and FUS^{P525L} MNs. The functional categories are represented with a character size proportional to the statistical significance of their enrichment.

(B) The histogram shows the fold enrichment of FUS binding sites, identified by re-analysis of data from Lagier-Tourenne et al. (2012), in different regions of pre-mRNAs, after normalization to average region size.

(C) Fraction of FUS bound protein-coding genes, which are also differentially expressed genes in FUS mutant MNs. A gene was considered bound if a FUS HITS-CLIP peak was found within its body; the analysis was repeated focusing only on specific pre-mRNA regions (Fisher's exact test; $*p < 0.05$; $***p < 0.001$).

(D) Validation of selected FUS-bound genes in MNs at day 12 + 7 by real-time qRT-PCR. Expression levels in FUS^{P525L}, FUS^{P525L}#2, and FUS^{P525L}(ht) are shown as relative to their respective isogenic FUS^{WT} controls, set to a value of 1. Histogram bars represent the average of at least three independent experiments and error bars indicate the SD (Student's t test; paired; two tails; $*p < 0.05$; $**p < 0.01$; $***p < 0.001$; n.s., $p > 0.05$).

(E) Venn diagram showing the overlap between differentially expressed genes in the present work and in a FUS mutant mouse (Scekic-Zahirovic et al., 2016). See also Figure S4.

for the 3′ UTR set (Figure S4C). Taken together, these results suggest that mRNAs bound by FUS in the 3′ UTR might be more susceptible to changes in FUS activity due to ALS mutations. We validated differential expression of selected FUS-bound mRNAs in mutant MNs (*TAF7*, *TAF15*, *GRIN2A*, *PCDH10*, and *CRIM1*) (Figures 2D and 3D).

To assess whether the changes in gene expression downstream of *FUS* ALS mutations are consistent with an animal

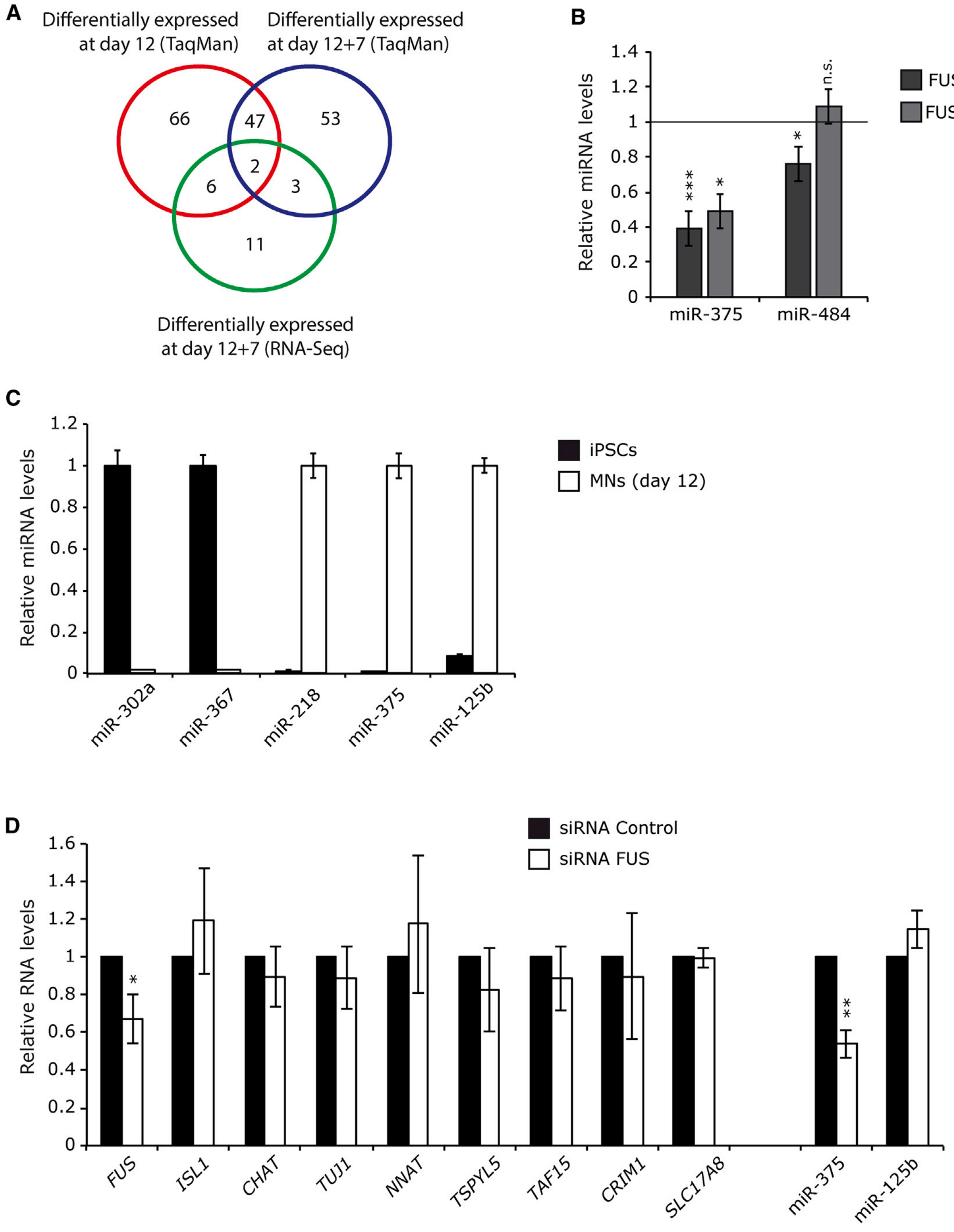

Figure 4. miR-375 Is Downregulated in FUS Mutant MNs

(A) Venn diagram showing the relations between differentially expressed miRNAs at different time points of MN maturation, as resulting from TaqMan array cards analysis in FUS^{WT} and FUS^{P525L} iPSC-derived MNs at day 12 and 12 + 7, and small RNA-seq at day 12 + 7 ($p < 0.05$).

(B) Validation of selected miRNAs by real-time qRT-PCR in MNs at day 12 + 7. Expression levels in FUS^{P525L} and FUS^{P525L}#2 are shown as relative to their respective isogenic FUS^{WT} controls, set to a value of 1. Histogram bars represent the average of at least four independent experiments and error bars indicate the SD (Student's t test; paired; two tails; $^{*}p < 0.05$; $^{***}p < 0.001$; n.s., $p > 0.05$).

(C) Real-time qRT-PCR analysis of the indicated miRNAs in FUS^{WT} undifferentiated iPSCs and MNs (day 12 of differentiation, unsorted). miR-302a and miR-367 are pluripotency miRNAs; miR-218 is an MN-enriched miRNA. For each miRNA, the sample with the highest

(legend continued on next page)

model exhibiting ALS features, we crossed our data with the transcriptome profiling of a recently described mouse carrying targeted deletion of the PY-NLS (Fus$^{\Delta NLS/\Delta NLS}$) (Scekic-Zahirovic et al., 2016). This mutation severely impairs the nuclear localization of FUS, mimicking the human P525L mutation and other truncations of the protein C-terminal. Among differentially expressed genes, 17 were downregulated and 8 were upregulated in both mutant mouse brain and human MNs (Figures 3E and S4D). The overlap was statistically significant both for upregulated and downregulated gene lists (p value for hypergeometric test <0.05). Interestingly, mRNA levels of *TAF15*, a *FUS* family member mutated in a subset of fALS patients (Couthouis et al., 2011), were significantly increased in both mouse (Scekic-Zahirovic et al., 2016) and human (Figure 3D). *TAF15* was among the transcripts directly bound by FUS (Lagier-Tourenne et al., 2012). These findings suggest that a possible crosstalk between *FUS* and *TAF15*, hypothesized in murine models, might be conserved in human.

FUS^{P525L} Mutation Impairs miR-375 Biogenesis in MNs by a Loss-of-Function Mechanism

Previous studies in cell lines have hypothesized a link between *FUS* mutations and the impairment of miRNA function (Emde et al., 2015; Morlando et al., 2012), but this was never directly investigated in human MNs. We performed miRNA profiling by small RNA sequencing (small RNA-seq) in FUS^{WT} and FUS^{P525L} MNs. Based on miRNA expression levels, samples could be clustered according to their *FUS* genotype (Figures S5A–S5C). Of the 573 miRNAs expressed in human MNs (day 12 + 7), 21 resulted downregulated and 11 upregulated in FUS^{P525L} mutant cells (FDR < 0.05) (Figure S5D; Table S1). We also analyzed to which extent the change in the miRNome is maintained at different time points. TaqMan array cards and small RNA-seq identified miR-375 and miR-484 as differentially expressed miRNAs at both day 12 and day 12 + 7 (Figure 4A; Table S2). These and other selected candidates were analyzed by real-time qRT-PCR in FUS^{P525L}, FUS^{P525L}#2, and FUS^{P525L}(ht) MNs, and their isogenic WT controls (Figures 4B, S5E, and S5F). Among them, miR-375 was consistently downregulated in both homozygous *FUS* mutant lines over at least four independent experiments (Figure 4B).

miR-375 has been recently described as a protective miRNA in MNs (Bhinge et al., 2016). Consistent with previous observations (Bhinge et al., 2016), miR-375 was highly upregulated in MNs compared with undifferentiated iPSCs (Figure 4C). To gain insights into the mechanisms underlying miR-375 downregulation in FUS^{P525L} MNs we transfected differentiating FUS^{WT} iPSCs with small interfering RNAs (siRNAs) targeting *FUS* and analyzed gene expression at day 12 of differentiation. In these conditions, *FUS* levels were reduced to about 60% compared with scramble siRNA-transfected cells (Figure 4D). We have previously shown that FUS localization in the nucleus in homozygous FUS^{P525L} cells is reduced to 50% of its normal levels, due to partial delocalization in the cytoplasm (Lenzi et al., 2015). Therefore, the decrease of FUS achieved by siRNA in WT cells is expected to reproduce possible loss of nuclear function effects of the mutation. FUS reduction did not affect differentiation, as assessed by *ISL1*, *CHAT*, and *TUJ1* marker analysis (Figure 4D). Levels of miR-375 were significantly reduced upon FUS knockdown (Figure 4D). Conversely, expression of selected genes among the most upregulated (*NNAT*, *TSPYL5*, and *TAF15*) or downregulated (*CRIM1* and *SLC17A8*) ones in FUS^{P525L} MNs was not affected by FUS knockdown (Figure 4D).

These results suggest that ALS mutations in the *FUS* gene might impair miR-375 production via a nuclear loss-of-function mechanism, while gain of toxic functions of the mutated protein might underlie the alteration of protein-coding genes expression.

miR-375 Target Genes in *FUS* Mutant MNs

To identify miR-375 targets in human MNs, we crossed mRNA expression data from the RNA-seq with predicted (TargetScan; Agarwal et al., 2015) and previously validated targets (miRTarBase; Chou et al., 2016). Eight mRNAs upregulated in FUS^{P525L} MNs were also miR-375 predicted targets (Figure 5A; Table S3), including *ELAVL4* (also known as *HuD*), which had been previously validated as a *bona fide* miR-375 target (Abdelmohsen et al., 2010). The increased expression of *ELAVL4* and other predicted targets (*PHLDA1*, *EBF3*, *B3GAT2*) in mutant MNs was validated by real-time qPCR (Figure 5B). The *ELAVL4* gene encodes for a neuron-specific RNA-binding protein (Bronicki and Jasmin, 2013). In mouse MNs, the transcript of the *NRN1* (*CPG15*) gene is among known targets of ELAVL4, which promotes *NRN1* mRNA accumulation by enhancing its stability (Akten et al., 2011). In line with this, we detected increased levels of *NRN1* in FUS^{P525L} MNs (Figure 5B).

We then noticed that the p53 gene (*TP53*) was a previously described target of miR-375 (Liu et al., 2013). *TP53* mRNA was unchanged or slightly upregulated,

expression has been used as the calibrator. Histogram bars represent the average of a technical replicate (n = 3) and error bars indicate the SD.

(D) Real-time qRT-PCR analysis in differentiated FUS^{WT} iPSCs (day 12) transfected with anti-FUS or control siRNAs. Histogram bars represent the expression relative to the siRNA control (average of three independent experiments). Error bars indicate the SD (Student's t test; paired; two tails; $^{*}p < 0.05$; $^{**}p < 0.01$; where not indicated $p > 0.05$). See also Figure S5.

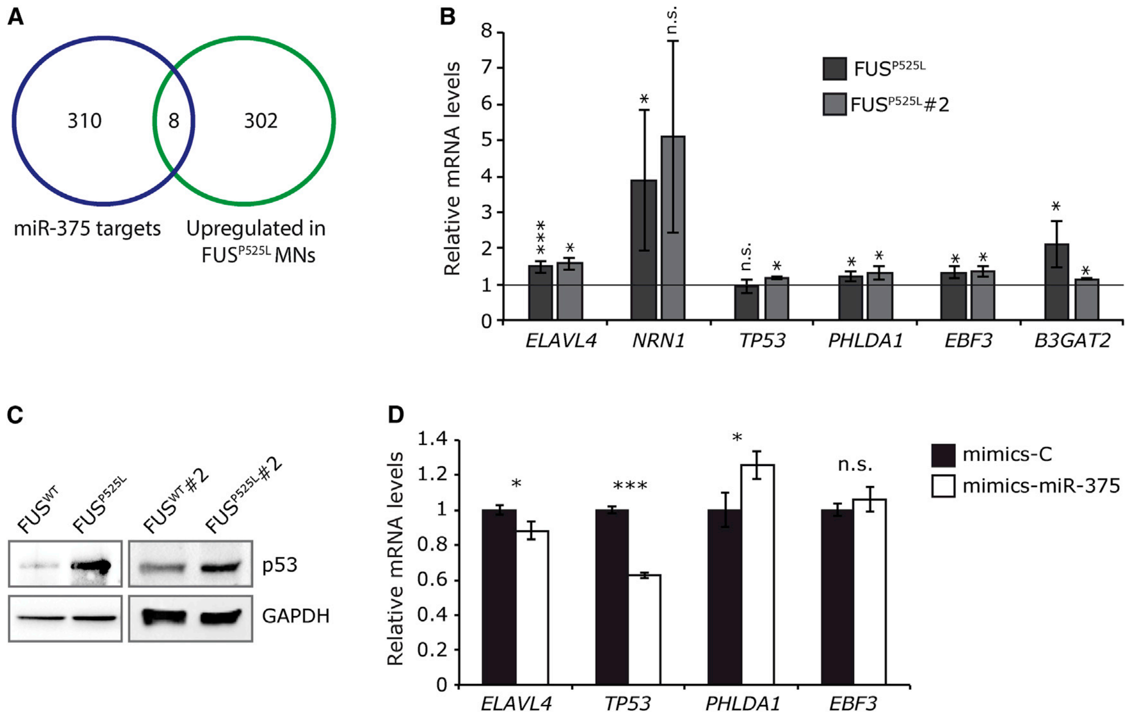

Figure 5. miR-375 Target Analysis

(A) Venn diagram showing the relations between predicted miR-375 targets and mRNAs upregulated in FUS^{P525L} MNs, as resulting from the RNA-seq analysis.

(B) Real-time qRT-PCR analysis in MNs at day 12 + 7. Expression levels in FUS^{P525L} and FUS^{P525L}#2 are shown as relative to their respective isogenic FUS^{WT} controls, set to a value of 1. Histogram bars represent the average of at least three independent experiments and error bars indicate the SD (Student's t test; paired; two tails; $*p < 0.05$; $***p < 0.001$; n.s., $p > 0.05$).

(C) Western blot analysis of p53 protein levels in FUS wild-type and mutant MNs at day 12 + 7. GAPDH is used as a housekeeping control.

(D) Real-time qRT-PCR analysis of the expression of the indicated genes in differentiated FUS^{P525L} iPSCs transfected with miR-375 miRNA mimics. Expression levels are relative to mimics control (mimics-C)-transfected samples. Histogram bars represent the average of at least three independent experiments and error bars indicate the SD (Student's t test; paired; two tails; $*p < 0.05$; $***p < 0.001$; n.s., $p > 0.05$).

respectively, in FUS^{P525L} and FUS^{P525L}#2 MNs (Figure 5B). In both lines, we detected an increase of p53 protein by western blot (Figure 5C). Among miR-375 targets, we noticed that *EBF3* and *PHLDA1* (also known as *TDAG51*) have been previously involved in the induction of apoptosis (Gomes et al., 1999; Zhao et al., 2006).

To assess whether changes in target mRNA levels could be explained by differences in miRNA levels, we transfected synthetic miR-375 mimics in FUS^{P525L} differentiated cells. We observed a significant decrease of *ELAVL4* and *TP53* mRNA levels compared with control-transfected cells (mimics-C) (Figure 5D). Since levels of *EBF3* and *PHLDA1* were not decreased, we hypothesize that other mechanisms might contribute to their upregulation in FUS mutant cells.

Collectively, these findings suggest that dysregulation of miR-375 in *FUS* mutant MNs may have an impact on RNA metabolism and survival due to aberrant increase of ELAVL4 and p53, respectively.

DISCUSSION

In this study we report the whole-transcriptome profile of *in-vitro*-derived human MNs with WT or mutant (P525L) *FUS* background. Our analysis was performed on two pairs of isogenic lines generated by gene editing. We therefore provide significant information on the changes in the transcriptome of the neuronal subtype primarily affected by ALS and due solely to the specific, ALS-linked, FUS^{P525L} mutation. This represents a major advance beyond previous work, in which the transcriptome of mixed populations of progenitor cells (composed for the most part of non-MN cells and derived from non-isogenic *FUS* control/mutant iPSCs) was profiled by exon array (Ichiyanagi et al., 2016).

We found that numerous differentially expressed genes belong to functional categories related to the cell adhesion pathway. Interestingly, this correlates with transcriptome analysis of postmortem laser-capture microdissected MNs

Please cite this article in press as: De Santis et al., *FUS* Mutant Human Motoneurons Display Altered Transcriptome and microRNA Pathways with Implications for ALS Pathogenesis, Stem Cell Reports (2017), https://doi.org/10.1016/j.stemcr.2017.09.004

from ALS patients, genome-wide association studies on several neurological diseases and differential gene expression in *C9ORF72* mutant cells (Aronica et al., 2015; Batra et al., 2016; Guio-Vega and Forero, 2017; Kotni et al., 2016). In the light of our findings, cell adhesion-related pathways might be considered as biomarkers and/or therapeutic targets in *FUS* ALS patients.

We also crossed our data with the transcriptome analysis from a recently reported murine model (Scekic-Zahirovic et al., 2016). Among genes commonly upregulated in both species we noticed *TAF15*, which is mutated in some ALS patients (Couthouis et al., 2011). TAF15 is a member of the FET family of RNA-binding proteins and is closely related to FUS. Similarly to FUS and TDP-43, upregulation of WT TAF15 causes neurodegeneration in *Drosophila* (Couthouis et al., 2011). Notably, *TAF15* levels were slightly increased in FUS null mice (Kino et al., 2015; Scekic-Zahirovic et al., 2016), but not in human MNs with reduced FUS levels (Figure 4D). This discrepancy might be explained by residual FUS protein in our RNAi experiment. A shift in TAF15 solubility and its localization into FUS-positive inclusions has been observed in frontotemporal lobar degeneration, but not in ALS (Neumann et al., 2011). Therefore, it remains unclear whether TAF15 upregulation in FUS mutant MNs contributes to ALS pathogenesis.

Changes in mRNA levels may be a direct consequence of the *FUS* mutation. Despite the fact that specific information on FUS-bound transcripts in human MNs is still missing, FUS CLIP-seq data from human brain cortex are available (Lagier-Tourenne et al., 2012). Our results suggest a possible direct effect of *FUS* mutations on those transcripts that are targeted by FUS on their 3′ UTR. Interestingly, levels of several transcripts were altered in the same direction in homozygous and heterozygous FUS^{P525L} MNs. The P525L mutation is inherited in an autosomal dominant way in ALS patients, and homozygous individuals have never been reported. Unexpectedly, in spinal cord tissue from heterozygous *FUS* ALS patients a near absence of nuclear FUS was observed in MNs, suggesting that both mutant and WT FUS can be sequestered within cytoplasmic inclusions (Vance et al., 2013). As the nuclear fraction of FUS in homozygous and heterozygous P525L cells is, respectively, 80% and 50% (Lenzi et al., 2015), the homozygous mutant could be regarded as representative of a more advanced stage of the disease. Mechanistically, toxic functions of mutant FUS might underlie the alteration of at least a subset of mRNAs, as suggested by knockdown experiments.

FUS mutations might also affect gene expression indirectly, for instance by altering miRNA levels. We found that miR-375 levels were consistently lower in MNs derived from two independent FUS^{P525L} lines. Bhinge et al. (2016) recently showed that miR-375 is enriched in human spinal MNs derived from embryonic stem cells. Interestingly, miR-375 overexpression protected MNs from DNA damage-induced apoptosis. Mechanistically, miR-375 may exert this function by targeting p53 (Bhinge et al., 2016; Liu et al., 2013). We show here that p53 and other pro-apoptotic miR-375 predicted targets are upregulated in *FUS* mutant MNs. Notably, spinal MNs of ALS patients have been shown to display higher levels of p53 protein, which could be involved in apoptosis-mediated neuronal death (Martin, 2000; Ranganathan and Bowser, 2010).

In FUS^{P525L} MNs we observed 40%–50% reduction in miR-375 levels. This is strikingly similar to the situation observed by Bhinge et al. (2016) in SMA MNs, in which miR-375 levels were reduced to 40%. Therefore, miR-375 dysregulation represents a common feature between two different MN diseases. While the molecular basis of miR-375 downregulation in SMA MNs remains currently unknown, we propose that ALS mutations causing FUS exclusion from the nucleus impair miR-375 production via a loss-of-function mechanism.

In addition to p53-induced apoptosis, miR-375 dysregulation might have an impact on other crucial pathways. Its decrease in FUS^{P525L} MNs is mirrored by an increase of its target ELAVL4, an RNA-binding protein playing multiple roles in neural development, function, and degeneration (Bronicki and Jasmin, 2013). ELAVL4 regulates the stability and/or localization of several target transcripts. We propose that FUS, through the miR-375/ELAVL4 axis, is hierarchically at the top of a regulatory network with a broader role in the RNA metabolism of MNs.

In conclusion, transcriptome analysis of isogenic FUS^{WT} and FUS^{P525L} *in-vitro*-derived human MNs provided an insight on target genes and pathways altered by ALS mutations in the cell type primarily affected by the disease.

EXPERIMENTAL PROCEDURES

Maintenance and Differentiation of Human iPSCs

Generation and maintenance of iPSC lines is described in Lenzi et al. (2015). The MN differentiation protocol has been modified from Hill et al. (2016). In brief, cells were differentiated in N2B27 medium supplemented with 1 μM all-*trans* retinoic acid (Sigma-Aldrich) and 1 μM SAG (Merck Millipore) for 12 days in the presence of 10 μM SB431542 and 100 nM LDN-193189 (both from Miltenyi Biotec) from day 0 to 6, and 5 μM DAPT and 4 μM SU-5402 (both from Sigma-Aldrich) from day 6 to 12. Cells were sorted at day 12 using a FACSAria III (BD Biosciences) and re-plated on poly-L-ornithine-coated dishes and laminin- coated dishes (both from Sigma-Aldrich) in Neural Medium. The *Hb9*:GFP reporter was stably integrated in the *AAVS1* locus, as described previously (Wainger et al., 2014).

RNA and Protein Analysis

Total RNA, extracted with the Quick-RNA MiniPrep (Zymo Research) and retrotranscribed with SuperScript VILO (Thermo Fisher Scientific) or miScript II RT (QIAGEN), was analyzed by real-time qRT-PCR with SYBR Green PowerUP (Thermo Fisher Scientific) or SYBR Green PCR Master Mix (QIAGEN). For miRNAs 384 array, RNA retrotranscribed using the TaqMan MicroRNA RT Kit was analyzed using the TaqMan Human MicroRNA Array A (Thermo Fisher Scientific). Primers sequences are reported in Table S4. Western blot analysis was carried out using anti-p53 (fl-393; Santa Cruz) and anti-GAPDH (sc-32233) antibodies.

RNA-Seq and Bioinformatics Analysis

Total RNA was sequenced on an Illumina HiSeq 2500 sequencing system using a TruSeq Stranded Total RNA Library Prep Kit with Ribo-Zero treatment (Illumina) or the TruSeq Small RNA Library (Illumina) at the Institute of Applied Genomics (Udine, Italy). An average of about 21 million 125 base pairs long paired-end reads or 17 million 50 base pairs long single-end reads were produced for each sample for RNA-seq or small RNA-seq, respectively. Bioinformatics analysis is described in detail in the Supplemental Experimental Procedures.

RNA-seq raw data have been deposited at the GEO (GEO: GSE94888).

Immunostaining

Immunostaining was performed with anti-Islet-1/2 (1:50, 39.4D5; DSHB) primary antibody and anti-mouse Alexa Fluor 488 (1:250, Thermo Fisher Scientific) goat secondary antibody. Images were acquired with an inverted iX73 microscope (Olympus).

FUS Knockdown and miRNA Mimics Transfection

Differentiating FUS^{WT} iPSCs were transfected at 8 and 10 days with 40 nM anti-FUS siRNAs (SI00070518, QIAGEN) or scramble control siRNAs (1027281, QIAGEN). FUS^{P525L} iPSCs, induced to differentiate into MNs for 14 days and seeded on Matrigel-coated plates, were transfected after 48 hr with 10 nM mirVana miRNA mimics (miR-375-3p MIMAT0000728; Negative Control No. 1 Cat. 4464058; Thermo Fisher Scientific). RNA was collected for real-time qRT-PCR analysis after 48 hr.

ACCESSION NUMBERS

The accession number for the RNA sequencing raw data reported in this paper is GEO: GSE94888.

SUPPLEMENTAL INFORMATION

Supplemental Information includes Supplemental Experimental Procedures, five figures, and four tables and can be found with this article online at https://doi.org/10.1016/j.stemcr.2017.09.004.

AUTHOR CONTRIBUTIONS

A.R. and R.D.S. conceived the project. R.D.S. generated *Hb9*:GFP iPSC lines, set up and optimized MN differentiation and isolation, and collected and analyzed RNA and protein samples. L.S. and V.A. contributed to iPSC culture and differentiation and RNA analysis. A.C. performed the bioinformatics analysis of the RNA-seq. G.P. set up and optimized the fluorescence-activated cell sorting analysis and sorting of MNs. V.d.T. acquired and analyzed microscopy images. A.R. and I.B. coordinated the work and wrote the paper.

ACKNOWLEDGMENTS

We thank Dr. Kevin Eggan (Harvard University) for providing the original MN differentiation protocol and the *Hb9*::GFP reporter construct. We are grateful to members of the Center for Life Nano Science and of the A.R. and I.B. laboratories for helpful discussion. This work was partially supported by AriSLA pilot grant 2016 "StressFUS" to A.R. and AriSLA full grant 2014 "ARCI," ERC-2013 - AdG 340172-MUNCODD, IIT "SEED," Epigen-Epigenomics Flagship Project, Human Frontiers Science Program Award RGP0009/2014, and Fondazione Roma to I.B.

Received: May 9, 2017
Revised: September 5, 2017
Accepted: September 6, 2017
Published: October 5, 2017

REFERENCES

Abdelmohsen, K., Hutchison, E.R., Lee, E.K., Kuwano, Y., Kim, M.M., Masuda, K., Srikantan, S., Subaran, S.S., Marasa, B.S., Mattson, M.P., and Gorospe, M. (2010). miR-375 inhibits differentiation of neurites by lowering HuD levels. Mol. Cell. Biol. *30*, 4197–4210.

Agarwal, V., Bell, G.W., Nam, J.-W., and Bartel, D.P. (2015). Predicting effective microRNA target sites in mammalian mRNAs. Elife *4*. http://dx.doi.org/10.7554/eLife.05005.

Akten, B., Kye, M.J., Hao, L.T., Wertz, M.H., Singh, S., Nie, D., Huang, J., Merianda, T.T., Twiss, J.L., Beattie, C.E., et al. (2011). Interaction of survival of motor neuron (SMN) and HuD proteins with mRNA cpg15 rescues motor neuron axonal deficits. Proc. Natl. Acad. Sci. USA *108*, 10337–10342.

Amin, N.D., Bai, G., Klug, J.R., Bonanomi, D., Pankratz, M.T., Gifford, W.D., Hinckley, C.A., Sternfeld, M.J., Driscoll, S.P., Dominguez, B., et al. (2015). Loss of motoneuron-specific microRNA-218 causes systemic neuromuscular failure. Science *350*, 1525–1529.

Aronica, E., Baas, F., Iyer, A., ten Asbroek, A.L., Morello, G., and Cavallaro, S. (2015). Molecular classification of amyotrophic lateral sclerosis by unsupervised clustering of gene expression in motor cortex. Neurobiol. Dis. *74*, 359–376.

Batra, R., Hutt, K., Vu, A., Rabin, S.J., Baughn, M.W., Libby, R.T., Hoon, S., Ravits, J., and Yeo, G.W. (2016). Gene expression signatures of sporadic ALS motor neuron populations. bioRxiv http://dx.doi.org/10.1101/038448.

Bentmann, E., Haass, C., and Dormann, D. (2013). Stress granules in neurodegeneration - lessons learnt from TAR DNA binding protein of 43 kDa and fused in sarcoma. FEBS J. *280*, 4348–4370.

Bhinge, A., Namboori, S.C., Bithell, A., Soldati, C., Buckley, N.J., and Stanton, L.W. (2016). MiR-375 is essential for human spinal motor neuron development and may be involved in motor neuron degeneration. Stem Cells *34*, 124–134.

Boulting, G.L., Kiskinis, E., Croft, G.F., Amoroso, M.W., Oakley, D.H., Wainger, B.J., Williams, D.J., Kahler, D.J., Yamaki, M., Davidow, L., et al. (2011). A functionally characterized test set of human induced pluripotent stem cells. Nat. Biotechnol. *29*, 279–286.

Bronicki, L.M., and Jasmin, B.J. (2013). Emerging complexity of the HuD/ELAVl4 gene; implications for neuronal development, function, and dysfunction. RNA *19*, 1019–1037.

Buratti, E., De Conti, L., Stuani, C., Romano, M., Baralle, M., and Baralle, F. (2010). Nuclear factor TDP-43 can affect selected microRNA levels. FEBS J. *277*, 2268–2281.

Chou, C.-H., Chang, N.-W., Shrestha, S., Hsu, S.-D., Lin, Y.-L., Lee, W.-H., Yang, C.-D., Hong, H.-C., Wei, T.-Y., Tu, S.-J., et al. (2016). miRTarBase 2016: updates to the experimentally validated miRNA-target interactions database. Nucleic Acids Res. *44*, D239–D247.

Couthouis, J., Hart, M.P., Shorter, J., Dejesus-Hernandez, M., Erion, R., Oristano, R., Liu, A.X., Ramos, D., Jethava, N., Hosangadi, D., et al. (2011). A yeast functional screen predicts new candidate ALS disease genes. Proc. Natl. Acad. Sci. USA *108*, 20881–20890.

D'Andrea, D., Grassi, L., Mazzapioda, M., and Tramontano, A. (2013). FIDEA: a server for the functional interpretation of differential expression analysis. Nucleic Acids Res. *41*, W84–W88.

Di Carlo, V., Grossi, E., Laneve, P., Morlando, M., Dini Modigliani, S., Ballarino, M., Bozzoni, I., and Caffarelli, E. (2013). TDP-43 regulates the microprocessor complex activity during in vitro neuronal differentiation. Mol. Neurobiol. *48*, 952–963.

Dormann, D., and Haass, C. (2011). TDP-43 and FUS: a nuclear affair. Trends Neurosci. *34*, 339–348.

Emde, A., Eitan, C., Liou, L.-L., Libby, R.T., Rivkin, N., Magen, I., Reichenstein, I., Oppenheim, H., Eilam, R., Silvestroni, A., et al. (2015). Dysregulated miRNA biogenesis downstream of cellular stress and ALS-causing mutations: a new mechanism for ALS. EMBO J. *34*, 2633–2651.

Gomes, I., Xiong, W., Miki, T., and Rosner, M.R. (1999). A proline- and glutamine-rich protein promotes apoptosis in neuronal cells. J. Neurochem. *73*, 612–622.

Guio-Vega, G.P., and Forero, D.A. (2017). Functional genomics of candidate genes derived from genome-wide association studies for five common neurological diseases. Int. J. Neurosci. *127*, 118–123.

Haramati, S., Chapnik, E., Sztainberg, Y., Eilam, R., Zwang, R., Gershoni, N., McGlinn, E., Heiser, P.W., Wills, A.-M., Wirguin, I., et al. (2010). miRNA malfunction causes spinal motor neuron disease. Proc. Natl. Acad. Sci. USA *107*, 13111–13116.

Hill, S.J., Mordes, D.A., Cameron, L.A., Neuberg, D.S., Landini, S., Eggan, K., and Livingston, D.M. (2016). Two familial ALS proteins function in prevention/repair of transcription-associated DNA damage. Proc. Natl. Acad. Sci. USA *113*, E7701–E7709.

Ichiyanagi, N., Fujimori, K., Yano, M., Ishihara-Fujisaki, C., Sone, T., Akiyama, T., Okada, Y., Akamatsu, W., Matsumoto, T., Ishikawa, M., et al. (2016). Establishment of in vitro fus-associated familial amyotrophic lateral sclerosis model using human induced pluripotent stem cells. Stem Cell Reports *6*, 496–510.

Kapeli, K., Pratt, G.A., Vu, A.Q., Hutt, K.R., Martinez, F.J., Sundararaman, B., Batra, R., Freese, P., Lambert, N.J., Huelga, S.C., et al. (2016). Distinct and shared functions of ALS-associated proteins TDP-43, FUS and TAF15 revealed by multisystem analyses. Nat. Commun. *7*, 12143.

Kawahara, Y., and Mieda-Sato, A. (2012). TDP-43 promotes microRNA biogenesis as a component of the Drosha and Dicer complexes. Proc. Natl. Acad. Sci. USA *109*, 3347–3352.

Kino, Y., Washizu, C., Kurosawa, M., Yamada, M., Miyazaki, H., Akagi, T., Hashikawa, T., Doi, H., Takumi, T., Hicks, G.G., et al. (2015). FUS/TLS deficiency causes behavioral and pathological abnormalities distinct from amyotrophic lateral sclerosis. Acta Neuropathol. Commun. *3*, 24.

Kiskinis, E., Sandoe, J., Williams, L.A., Boulting, G.L., Moccia, R., Wainger, B.J., Han, S., Peng, T., Thams, S., Mikkilineni, S., et al. (2014). Pathways disrupted in human ALS motor neurons identified through genetic correction of mutant SOD1. Cell Stem Cell *14*, 781–795.

Kong, Y., Liang, X., Liu, L., Zhang, D., Wan, C., Gan, Z., and Yuan, L. (2015). High throughput sequencing identifies microRNAs mediating α-synuclein toxicity by targeting neuroactive-ligand receptor interaction pathway in early stage of drosophila Parkinson's disease model. PLoS One *10*, e0137432.

Kotni, M.K., Zhao, M., and Wei, D.-Q. (2016). Gene expression profiles and protein-protein interaction networks in amyotrophic lateral sclerosis patients with C9orf72 mutation. Orphanet J. Rare Dis. *11*, 148.

Kwiatkowski, T.J., Bosco, D.A., Leclerc, A.L., Tamrazian, E., Vanderburg, C.R., Russ, C., Davis, A., Gilchrist, J., Kasarskis, E.J., Munsat, T., et al. (2009). Mutations in the FUS/TLS gene on chromosome 16 cause familial amyotrophic lateral sclerosis. Science *323*, 1205–1208.

Kye, M.J., and Gonçalves, I.D.C.G. (2014). The role of miRNA in motor neuron disease. Front. Cell. Neurosci. *8*, 15.

Lagier-Tourenne, C., Polymenidou, M., Hutt, K.R., Vu, A.Q., Baughn, M., Huelga, S.C., Clutario, K.M., Ling, S.-C., Liang, T.Y., Mazur, C., et al. (2012). Divergent roles of ALS-linked proteins FUS/TLS and TDP-43 intersect in processing long pre-mRNAs. Nat. Neurosci. *15*, 1488–1497.

Lenzi, J., De Santis, R., de Turris, V., Morlando, M., Laneve, P., Calvo, A., Caliendo, V., Chiò, A., Rosa, A., and Bozzoni, I. (2015). ALS mutant FUS proteins are recruited into stress granules in induced pluripotent stem cells (iPSCs) derived motoneurons. Dis. Model. Mech. *8*, 755–766.

Lenzi, J., Pagani, F., De Santis, R., Limatola, C., Bozzoni, I., Di Angelantonio, S., and Rosa, A. (2016). Differentiation of control and ALS mutant human iPSCs into functional skeletal muscle cells, a tool for the study of neuromuscular diseases. Stem Cell Res. *17*, 140–147.

Ling, S.-C., Polymenidou, M., and Cleveland, D.W. (2013). Converging mechanisms in ALS and FTD: disrupted RNA and protein homeostasis. Neuron *79*, 416–438.

Liu, Y., Xing, R., Zhang, X., Dong, W., Zhang, J., Yan, Z., Li, W., Cui, J., and Lu, Y. (2013). miR-375 targets the p53 gene to regulate cellular response to ionizing radiation and etoposide in gastric cancer cells. DNA Repair (Amst) *12*, 741–750.

Please cite this article in press as: De Santis et al., *FUS* Mutant Human Motoneurons Display Altered Transcriptome and microRNA Pathways with Implications for ALS Pathogenesis, Stem Cell Reports (2017), https://doi.org/10.1016/j.stemcr.2017.09.004

Martin, L.J. (2000). p53 is abnormally elevated and active in the CNS of patients with amyotrophic lateral sclerosis. Neurobiol. Dis. *7*, 613–622.

Morlando, M., Dini Modigliani, S., Torrelli, G., Rosa, A., Di Carlo, V., Caffarelli, E., and Bozzoni, I. (2012). FUS stimulates microRNA biogenesis by facilitating co-transcriptional Drosha recruitment. EMBO J. *31*, 4502–4510.

Neumann, M., Bentmann, E., Dormann, D., Jawaid, A., Dejesus-Hernandez, M., Ansorge, O., Roeber, S., Kretzschmar, H.A., Munoz, D.G., Kusaka, H., et al. (2011). FET proteins TAF15 and EWS are selective markers that distinguish FTLD with FUS pathology from amyotrophic lateral sclerosis with FUS mutations. Brain *134*, 2595–2609.

Orozco, D., and Edbauer, D. (2013). FUS-mediated alternative splicing in the nervous system: consequences for ALS and FTLD. J. Mol. Med. *91*, 1343–1354.

Ranganathan, S., and Bowser, R. (2010). p53 and cell cycle proteins participate in spinal motor neuron cell death in ALS. Open Pathol. J. *4*, 11–22.

Renton, A.E., Chiò, A., and Traynor, B.J. (2014). State of play in amyotrophic lateral sclerosis genetics. Nat. Neurosci. *17*, 17–23.

Sances, S., Bruijn, L.I., Chandran, S., Eggan, K., Ho, R., Klim, J.R., Livesey, M.R., Lowry, E., Macklis, J.D., Rushton, D., et al. (2016). Modeling ALS with motor neurons derived from human induced pluripotent stem cells. Nat. Neurosci. *16*, 542–553.

Scekic-Zahirovic, J., Sendscheid, O., El Oussini, H., Jambeau, M., Sun, Y., Mersmann, S., Wagner, M., Dieterlé, S., Sinniger, J., Dirrig-Grosch, S., et al. (2016). Toxic gain of function from mutant FUS protein is crucial to trigger cell autonomous motor neuron loss. EMBO J. *35*, 1077–1097.

Tollervey, J.R., Curk, T., Rogelj, B., Briese, M., Cereda, M., Kayikci, M., König, J., Hortobágyi, T., Nishimura, A.L., Župunski, V., et al. (2011). Characterizing the RNA targets and position-dependent splicing regulation by TDP-43. Nat. Neurosci. *14*, 452–458.

Vance, C., Rogelj, B., Hortobágyi, T., De Vos, K.J., Nishimura, A.L., Sreedharan, J., Hu, X., Smith, B., Ruddy, D., Wright, P., et al. (2009). Mutations in FUS, an RNA processing protein, cause familial amyotrophic lateral sclerosis type 6. Science *323*, 1208–1211.

Vance, C., Scotter, E.L., Nishimura, A.L., Troakes, C., Mitchell, J.C., Kathe, C., Urwin, H., Manser, C., Miller, C.C., Hortobágyi, T., et al. (2013). ALS mutant FUS disrupts nuclear localization and sequesters wild-type FUS within cytoplasmic stress granules. Hum. Mol. Genet. *22*, 2676–2688.

Wainger, B.J., Kiskinis, E., Mellin, C., Wiskow, O., Han, S.S.W., Sandoe, J., Perez, N.P., Williams, L.A., Lee, S., Boulting, G., et al. (2014). Intrinsic membrane hyperexcitability of amyotrophic lateral sclerosis patient-derived motor neurons. Cell Rep. *7*, 1–11.

Zhao, L.Y., Niu, Y., Santiago, A., Liu, J., Albert, S.H., Robertson, K.D., and Liao, D. (2006). An EBF3-mediated transcriptional program that induces cell cycle arrest and apoptosis. Cancer Res. *66*, 9445–9452.

Stem Cell Reports, Volume *9*

Supplemental Information

FUS Mutant Human Motoneurons Display Altered Transcriptome and microRNA Pathways with Implications for ALS Pathogenesis

Riccardo De Santis, Laura Santini, Alessio Colantoni, Giovanna Peruzzi, Valeria de Turris, Vincenzo Alfano, Irene Bozzoni, and Alessandro Rosa

SUPPLEMENTAL INFORMATION

FUS mutant human motoneurons display altered transcriptome and microRNA pathways with implications for ALS pathogenesis

De Santis et al.

SUPPLEMENTAL FIGURES AND TABLES

Figure S1

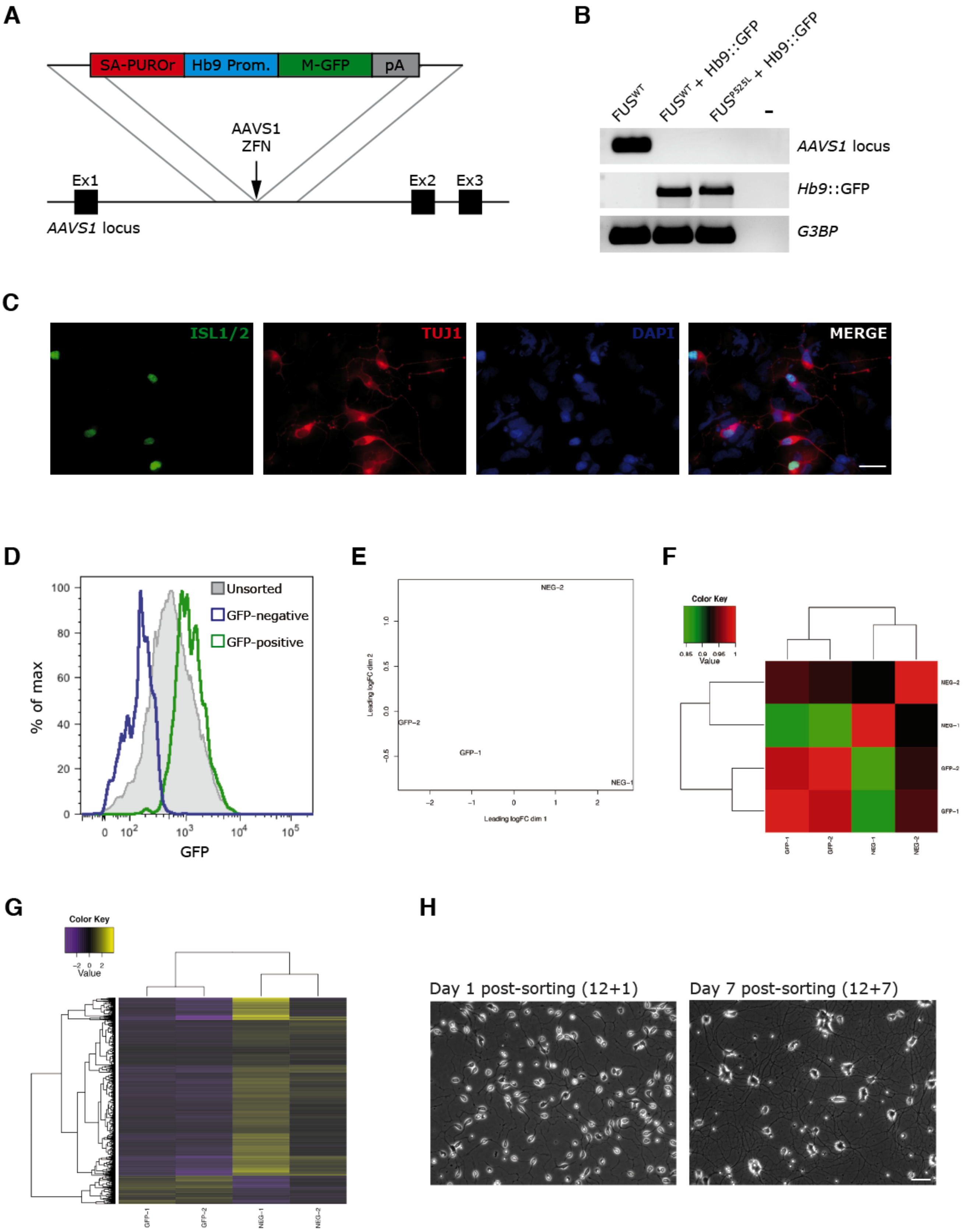
A
SA-PUROr
Hb9 Prom.
M-GFP
pA
AAVS1
ZFN
Ex1
Ex2
Ex3
AAVS1 locus
B
FUS^WT
FUS^WT + Hb9::GFP
FUS^P525L + Hb9::GFP
-
AAVS1 locus
Hb9::GFP
G3BP
C
ISL1/2
TUJ1
DAPI
MERGE
D
Unsorted
GFP-negative
GFP-positive
% of max
100
80
60
40
20
0
0
10^2
10^3
10^4
10^5
GFP
E
NEG-2
GFP-2
GFP-1
NEG-1
Leading logFC dim 2
1.0
0.5
0.0
-0.5
-2
-1
0
1
2
Leading logFC dim 1
F
Color Key
0.85
0.9
0.95
1
Value
NEG-2
NEG-1
GFP-2
GFP-1
GFP-1
GFP-2
NEG-1
NEG-2
G
Color Key
-2
0
2
Value
GFP-1
GFP-2
NEG-1
NEG-2
H
Day 1 post-sorting (12+1)
Day 7 post-sorting (12+7)

Figure S1. MN differentiation and sorting. Related to Figure 1

(A) Schematic representation of the *Hb9*::GFP reporter system, inserted in the *AAVS1* locus by gene editing with zinc-finger nucleases (ZFN). A specific break introduced by ZFN in the *AAVS1* locus (arrow) is repaired by homologous recombination, introducing a puromycin resistance gene spliced in frame with *AAVS1* (SA-PUROr) and a membrane-localized GFP (M-GFP) coding sequence under the control of the *Hb9* promoter. pA indicates cleavage and polyadenylation signal site. (B) End-point PCR analysis on the genomic DNA of iPSCs before ($\mathrm{FUS^{WT}}$) or after ($\mathrm{FUS^{WT}}$+*Hb9*::GFP; $\mathrm{FUS^{P525L}}$+*Hb9*::GFP) transfection with *AAVS1* ZFNs and *Hb9*::GFP reporter system. Primers annealed to the unmodified *AAVS1* locus (top), to the reporter pA and the AAVS1 locus (outside of the sequence corresponding to the homology arm region; middle) or to an unrelated genomic locus as a control, *G3BP* (bottom). (C) Immunostaining analysis of ISL1/2 and TUJ1 markers of cells differentiated for 12 days as in Fig. 1A, dissociated, re-plated on laminin-coated dishes and cultured for 2 additional days in Neural Medium. DAPI was used to stain nuclei. Widefield images acquired at a Zeiss Axiovert A1 microscope with a 40X objective. Scalebar: 20µm. (D) GFP-positive and -negative cells were analyzed by FACS to check the purity of the sorted samples. Plot overlay show the purity of isolated populations compared to unsorted sample. (E) MDS plot showing clustering of GFP-positive and -negative samples based on log2-transformed CPM values obtained by RNA-Seq analysis. (F) Hierarchical clustering and Pearson correlation matrix of GFP-positive and -negative samples based on log2-transformed CPM values obtained by RNA-Seq analysis. (G) Heatmap representing RNA-Seq-derived expression levels of genes that are differentially expressed between GFP-positive and -negative cells collected after sorting (3 independent experiments). Plotted values correspond to mean-centered log2-transformed RPKM values. (H) Phase contrast images of cells sorted at day 12 for GFP expression and further cultured for 1 (left panel) and 7 (right panel) days on laminin-coated dishes. Scalebar: 50µm

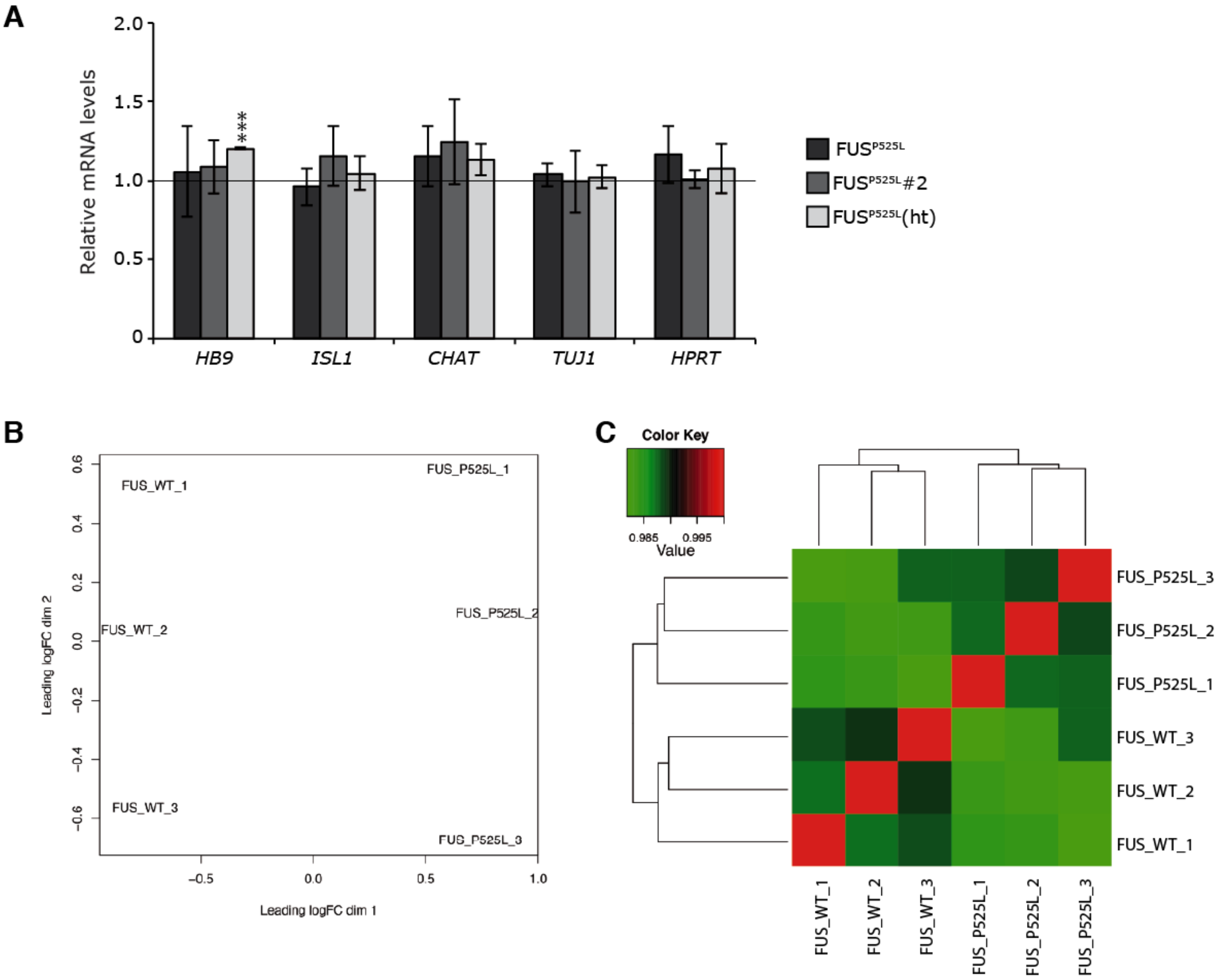

D

WT	mut	logFC	FDR	Gene
15,06239306	12,8626685	-0,225370876	0,337140521	*FUS*
13,70944313	13,91139185	0,028991541	0,980872563	*C9ORF72*
41,52603942	41,1847425	-0,018591906	0,986091697	*SOD1*
13,47852002	13,72464251	0,026604731	0,980919096	*TARDBP*
50,8394313	57,349796	0,176772149	0,620350018	*PFN1*
78,80149164	73,31606647	-0,10446142	0,832819031	*VCP*
20,83492422	21,70781378	0,059418114	0,953240486	*OPTN*
6,561830792	6,383976681	-0,043784725	0,973883291	*SQSTM1*
22,30248359	21,45401515	-0,057279194	0,957875144	*UBQLN2*
75,62437945	76,42145168	0,022591984	0,984419358	*MATR3*

Figure S2. FUS^{WT} and FUS^{P525L} iPSC generate MNs with comparable efficiency. Related to Figure 2
(A) Real-time qRT-PCR analysis of the expression of the indicated genes in purified MNs (day12+7). Expression levels in FUS^{P525L}, FUS^{P525L}#2 and FUS^{P525L}(ht) are shown as relative to their respective isogenic FUS^{WT} controls, set to a value of 1.

Histogram bars represent the average of at least 3 independent experiments and error bars indicate the standard deviation (Student's t-test; paired; two tails; ***= $p<0.001$; $p>0.05$ for all other genes). *HB9*, *ISL1* and *CHAT* are MN markers. *TUJ1* is a pan-neuronal marker and *HPRT* is a housekeeping control. (B) MDS plot showing clustering of FUS^{WT} and FUS^{P525L} samples based on log2-transformed CPM values obtained by RNA-Seq analysis. (C) Hierarchical clustering and Pearson correlation matrix of FUS^{WT} and FUS^{P525L} samples based on log2-transformed CPM values obtained by RNA-Seq analysis. (D) Table showing the expression levels (RPKM) of ALS associated genes in RNA-Seq analysis. LogFC indicates log2 fold change in FUS^{WT} vs FUS^{P525L} comparison.

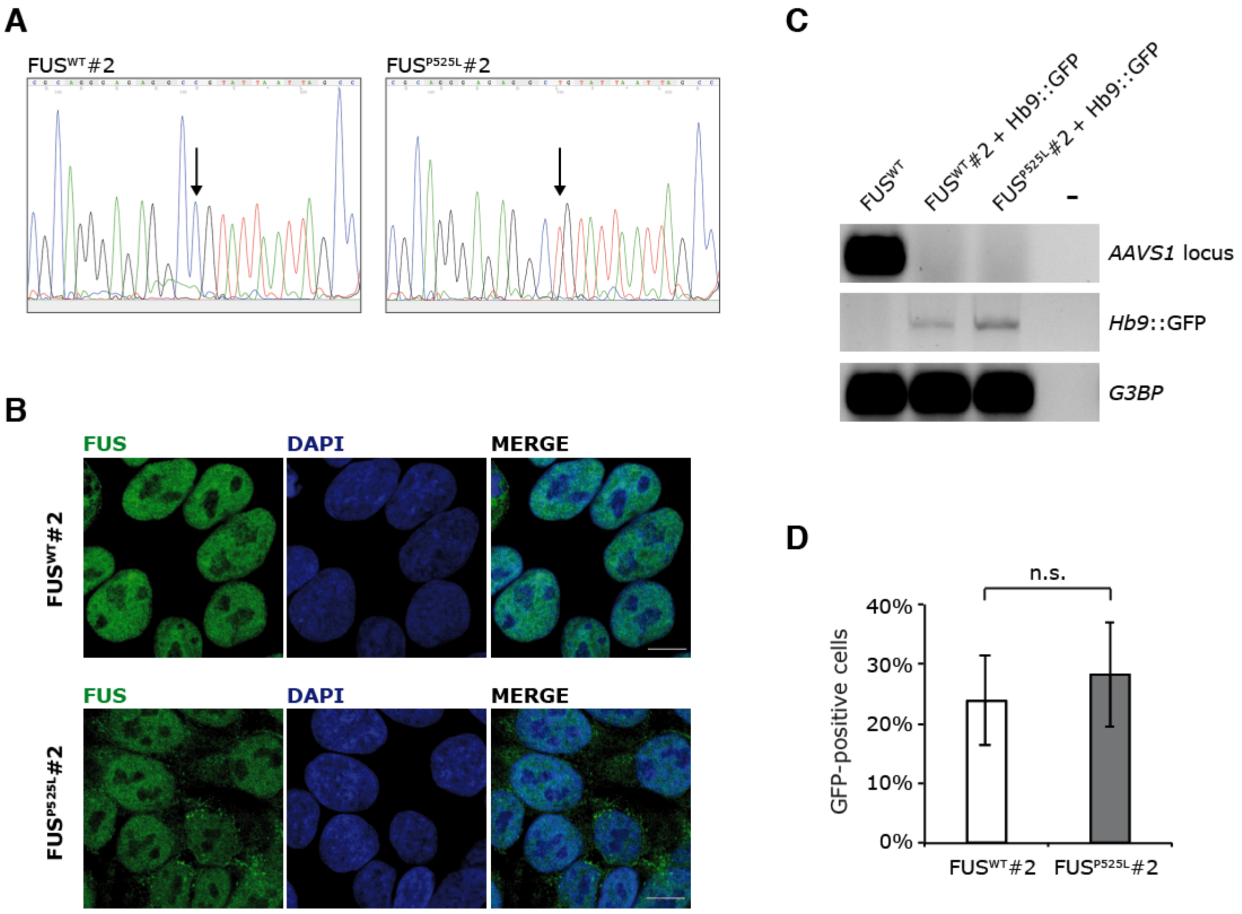

Figure S3. Characterization of FUS^{WT}#2 and FUS^{P525L}#2 iPSC lines. Related to Figure 2

(A) Sequencing results from FUS^{WT}#2 and FUS^{P525L}#2 iPSC lines. FUS^{P525L}#2 iPSCs were modified by TALEN-directed HDR with the strategy described in (Lenzi et al., 2015). The arrows indicate the targeted nucleotide in codon 525 (C, wild type; T, mutant). (B) Immunostaining showing intracellular localization of WT and mutant FUS proteins in iPSCs. Scale bar: 10 µm. (C) End-point PCR analysis on the genomic DNA of FUS^{WT}#2 and FUS^{P525L}#2 iPSC lines. iPSCs before transfection with *AAVS1* ZFNs and *Hb9*::GFP reporter system are used as control (FUS^{WT}). Primers annealed to the unmodified *AAVS1* locus (top), to the reporter pA and the *AAVS1* locus (outside of the sequence corresponding to the homology arm region; middle) or to an unrelated genomic locus as a control, *G3BP* (bottom). (D) Schematic representation of flow cytometry analysis of the fraction of GFP-positive cells at day 12. Histogram bars represent the average of 4 independent experiments and error bars indicate the standard deviation (Student's t-test; unpaired; two-tails; n.s.= p>0.05).

A

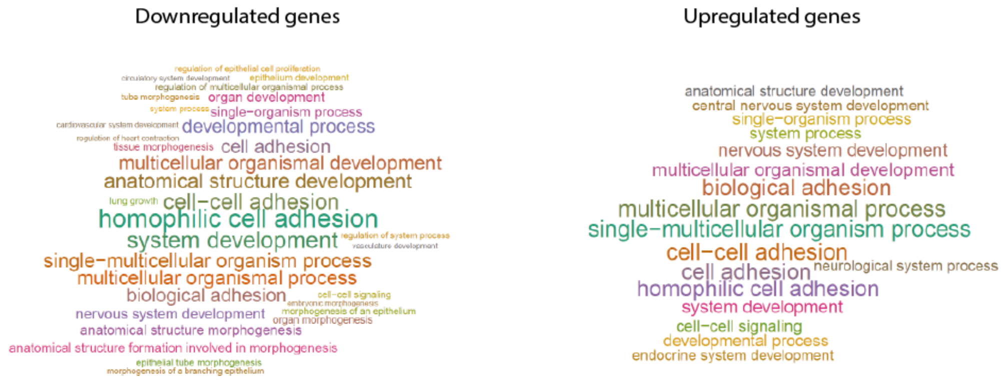
Downregulated genes

Upregulated genes

B

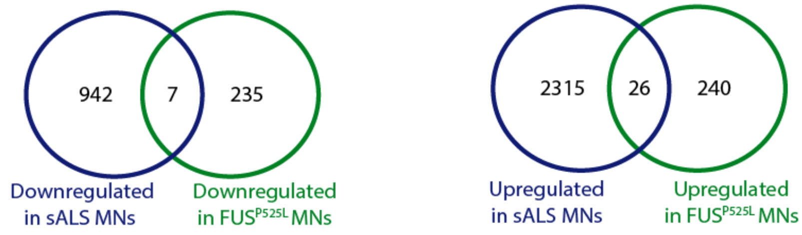

Downregulated in sALS and FUS^{P525L} MNs	*MURC; SLC44A5; GPR149; C11orf87; GAL3ST4; TCERG1L; SLITRK1*
Upregulated in sALS and FUS^{P525L} MNs	*CNGA3; CRABP1; SULF2; NPNT; GBX2; CDH7; ZNF703; HOXB7; COMT; RFTN1; SEMA3E; PLAGL1; TMEM257; GSTO2; ZNF578; EBF3; SLCO1A2; CTNNA3; PRR11; NXPH4; SH2B3; GCNT4; COL17A1; EFCAB13; ASCL1; SALL3*

C

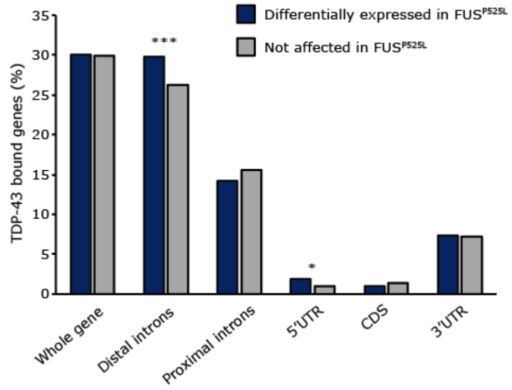

D

Downregulated concordant	*CHODL; CRIM1; CADM2; C6orf62; RSPO2; KCNK9; C11orf87; LGI3; KCND2; IL13RA1; MTURN; BAALC; NXPH1; PDE1C; GRK3; OXCT1; FGF13*
Downregulated discordant	*ZNF267; SULF1; TMX4*
Upregulated concordant	*NPTX1; ASIC4; TAF15; NHLH2; UPF3B; PSPC1; ONECUT3; FLRT2*
Upregulated discordant	*SHISA6; NTS; KCNIP1; RYR3; ATP1B1; PPP2R2C; HOXB3; ARPP21; OPCML; FABP3*

Figure S4. Bioinformatics analysis of differentially expressed genes in FUS^{WT} and FUS^{P525L} MNs. Related to Figure 3
(A) Word cloud generated by FIDEA representing GO Biological Process terms enriched in the list of genes that are downregulated (left panel) or upregulated (right panel) in FUS^{P525L} MNs. The functional categories are represented with a character size proportional to the statistical significance of their enrichment. (B) Top: Venn diagrams showing the overlap between downregulated and upregulated genes in the present work and in MNs isolated by laser capture from sALS patients (Batra et al., 2016). Bottom: table of commonly upregulated and downregulated genes. (C) Fraction of TDP-43 bound protein-coding genes (identified by Tollervey et al., 2011) which are also differentially expressed genes in FUS mutant MNs. A gene was considered to be bound if a TDP-43 iCLIP peak was found within its body; the analysis was repeated focusing only on specific pre-mRNA regions (Fisher's exact test; *= $p<0.05$; ***=$p<0.001$). (D) Table showing the identity of the genes indicated in the Venn diagram of Figure 3E (overlap between differentially expressed genes in the present work and in a FUS mutant mouse; Scekic-Zahirovic et al., 2016).

Figure S5

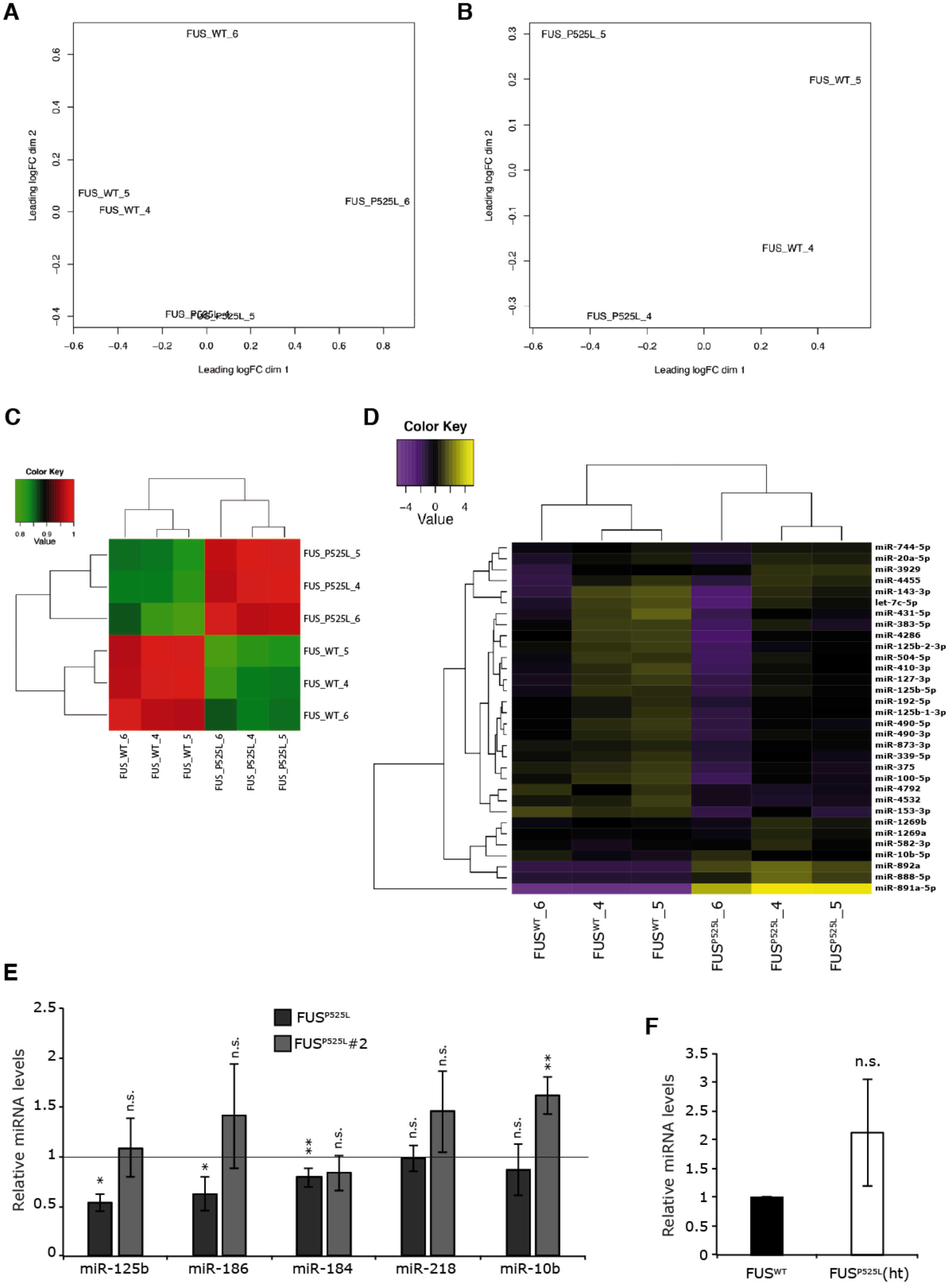
A
Leading logFC dim 1
Leading logFC dim 2
FUS_WT_6
FUS_WT_5
FUS_WT_4
FUS_P525L_6
FUS_P525L_4
FUS_P525L_5
B
Leading logFC dim 1
Leading logFC dim 2
FUS_P525L_5
FUS_WT_5
FUS_WT_4
FUS_P525L_4
C
Color Key
Value
0.8
0.9
1
FUS_P525L_5
FUS_P525L_4
FUS_P525L_6
FUS_WT_5
FUS_WT_4
FUS_WT_6
D
Color Key
Value
−4
0
4
miR-744-5p
miR-20a-5p
miR-3929
miR-4455
miR-143-3p
let-7c-5p
miR-431-5p
miR-383-5p
miR-4286
miR-125b-2-3p
miR-504-5p
miR-410-3p
miR-127-3p
miR-125b-5p
miR-192-5p
miR-125b-1-3p
miR-490-5p
miR-490-3p
miR-873-3p
miR-339-5p
miR-375
miR-100-5p
miR-4792
miR-4532
miR-153-3p
miR-1269b
miR-1269a
miR-582-3p
miR-10b-5p
miR-892a
miR-888-5p
miR-891a-5p
FUSWT_6
FUSWT_4
FUSWT_5
FUSP525L_6
FUSP525L_4
FUSP525L_5
E
Relative miRNA levels
FUSP525L
FUSP525L#2
miR-125b
miR-186
miR-184
miR-218
miR-10b
*
n.s.
**
F
Relative miRNA levels
n.s.
FUSWT
FUSP525L(ht)

Figure S5. Small RNA-Seq analysis. Related to Figure 4

(A) MDS plot showing clustering of FUS^{WT} and FUS^{P525L} samples based on log2-transformed CPM values obtained by small RNA-Seq analysis. (B) The same plot was drawn after removing samples from one differentiation experiment to appreciate the pairing of samples originated from the remaining two experiments. (C) Hierarchical clustering and Pearson correlation matrix of FUS^{WT} and FUS^{P525L} samples based on log2-transformed CPM values obtained by small RNA-Seq analysis. (D) Heatmap representing small RNA-Seq-derived expression levels of miRNAs that are differentially expressed between FUS^{WT} and FUS^{P525L} iPSC-derived MNs at day 12+7 (3 independent experiments). Plotted values correspond to mean-centered log2-transformed CPM values. (E) Analysis of the expression of selected miRNAs in MNs at day 12+7 by real time qRT-PCR. Expression levels in FUS^{P525L} and FUS^{P525L}#2 are shown as relative to their respective isogenic FUS^{WT} controls, set to a value of 1. Histogram bars represent the average of at least 3 independent experiments and error bars indicate the standard deviation (Student's t-test; paired; two tails; *= $p<0.05$; **= $p<0.01$; n.s.= $p>0.05$). (F) Analysis of the expression of miR-375 in MNs at day 12+7 by real time qRT-PCR. Expression levels in FUS^{P525L}(ht) are shown as relative to its isogenic FUS^{WT} control. Histogram bars represent the average of at least 3 independent experiments and error bars indicate the standard deviation (Student's t-test; paired; two tails; n.s.= $p>0.05$).

Groups	**Total**	**Elements**
day 12; day 12+7; small-seq(p-value<0,05)	2	miR-375
		miR-484
day 12+7; small-seq(p-value<0,05)	3	miR-129-3p
		miR-125b-5p
		miR-139-5p
day 12; small-seq(p-value<0,05)	6	miR-504-5p
		miR-10b-5p
		miR-149-5p
		miR-25-3p
		miR-192-5p
		miR-185-5p
day 12; day 12+7	47	miR-331
		miR-106a
		miR-574-3p
		miR-93
		miR-652
		miR-124a
		miR-486
		miR-193b
		miR-20a
		miR-532
		miR-627
		miR-483-5p
		miR-200c
		miR-16
		miR-216b
		miR-886-5p
		miR-26b
		miR-660
		miR-140-3p
		miR-31
		miR-454
		miR-30b
		miR-216a
		miR-330
		miR-218
		let-7g

		miR-133a
		miR-186
		miR-365
		miR-92a
		miR-191
		miR-184
		miR-10a
		miR-26a
		miR-628-5p
		miR-125a-5p
		miR-146b
		miR-28-3p
		miR-708
		miR-886-3p
		miR-20b
		miR-296
		miR-422a
		miR-425-5p
		miR-103
		miR-95
		miR-598

Table S2. Differentially expressed miRNAs in FUS^{WT} vs FUS^{P525L} MNs (Taqman Array Cards). Related to Figure 4

Name	**Sequence**
AAVS1 FW	CAGGGCCGGTTAATGTGGCT
AAVS1 HB9 FW	CACTCTCGGCATGGACGAGCTG
AAVS1 HB9 RV	CCAAAAGGCAGCCTGGTAGACAG
AAVS1 RV	GGGTTAGACCCAATATCAGG
ATP1B1 FW	AAGCCCACATATCAGGACCGAG
ATP1B1 RV	TGCCTCATAGCTCTTGGGATCAT
ATP5O FW	ACTCGGGTTTGACCTACAGC
ATP5O RV	GGTACTGAAGCATCGCACCT
B3GAT2 FW	TCTTCCAGGAGATGCGAACCAC
B3GAT2 RV	ACAACTTTGCCGTTTTCCACCA
CDH7 FW	GGAGCCCTGATAGCCATACTCG
CDH7 RV	GGTTTCTCAGTGCAGCCATGTC
ChAT FW	CTCAGCTACAAGGCCCTGCT
CHAT RV	ACCAGCGTGTCCTGGGTATG
CRIM1 FW	TCGAACCTGCAGCAATCCCTTT
CRIM1 RV	AGAGAACTGGACTTCACAGCGG
EBF3 FW	TCTACGAGGGCCAGGACAAGA
EBF3 RV	GGTCTGAGGGCGTTTCGTTTC
ELAVL4 FW	CAACCCCAGCCAGAAGTCCA
ELAVL4 RV	AGCCTGAACCTCTGAGCCTG
G3BP1 FW	CCAGGATTTGGAGTGGGAAGGG
G3BP1 RV	CAGACTGGGGTCATACTCCAAG
GAPDH FW	GGAAGGTGAAGGTCGGAGTC
GAPDH REV	TTACCAGAGTTAAAAGCAGCCC
GRIN2A FW	GGTCAGCCTGAAAACGGGGAA
GRIN2A RV	TGTACCCACTCCCGATGGTCA
HB9 FW	GAGACCCAGGTGAAGATTTG
HB9 RV	CCTTCTGTTTCTCCGCTTCC
HPRT FW	GCCCTGGCGTCGTGATTAGT
HPRT RV	GGCCTCCCATCTCCTTCATCA
ISL-1 FW	TACAAAGTTACCAGCCACC
ISL-1 RV	GGAAGTTGAGAGGACATTGA
LRFN2 FW	CCGGGTGAAGATGTACCAGCT
LRFN2 RV	TGAGTGTCGTGGCTGTGTCAT
NANOG FW	CCAAATTCTCCTGCCAGTGAC
NANOG RV	CACGTGGTTTCCAAACAAGAAA
NNAT FW	TGCTCATCATCGGCTGGTACA
NNAT RV	ACACCGTGTATGCCAGCTTCT
NRN1 FW	GGCTTTTCGGACTGTTTGCTCA
NRN1 RV	ATCCTCCCAGTATGTGCACACG
NXPH2 FW	TCCCCTGCGCCTGTTTGTTAAA
NXPH2 RV	CCAATGGCTCCTGAATCTCCGT
PAX FW	ATGTGTGAGTAAAATTCTGGGCA
PAX RV	GCTTACAACTTCTGGAGTCGCTA

PHLDA1 FW	CAGAGGGCAAGGAGATCGACTT
PHLDA1 RV	GGCCTGACGATTCTTGTACTGC
SHISA6 FW	CGAGAACAAGTACGACCCGGA
SHISA6 RV	AGCCCTGTGGATGTTCATCTCC
SLC17A8 FW	ACGCCGTGGGAGATTCTTTGG
SLC17A8 RV	TGATGTAACGCTTGGGGAGGC
TAF15 FW	GGGTCACAGGGAGGAGGTAGA
TAF15 RV	CCATAATCCCTGTGACCACCAAAA
TAF7 FW	GGGCGTCATGGAATCGTCAGA
TAF7 RV	TCAAGCTTTCCATAACACAGGGCA
TP53 FW	TGGCCATCTACAAGCAGTCACA
TP53 RV	CGGATAAGATGCTGAGGAGGGG
TP53I3 FW	CTCACCGCCTTCCAGCTGTT
TP53I3 RV	CGGGTGAGTTGGATAGCAGCT
TSPYL5 FW	GGCCCAATCCCTTGCAGTTCT
TSPYL5 RV	TGCTTTCCTGGACCTTGCCTG
TUJ1 FW	CCCGGAACCATGGACAGTGT
TUJ1 RV	TGACCCTTGGCCCAGTTGTT
Hs_SNORD25_11 miScript Primer Assay	(SNORD25 small nucleolar RNA, C/D box 25)
Hs_miR-125b_1 miScript Primer Assay	MIMAT0000423: 5'UCCCUGAGACCCUAACUUGUGA
Hs_miR-10b_3 miScript Primer Assay	MIMAT0000254: 5'UACCCUGUAGAACCGAAUUUGUG
Hs_miR-184_1 miScript Primer Assay	MIMAT0000454: 5'UGGACGGAGAACUGAUAAGGGU
Hs_miR-186_1 miScript Primer Assay	MIMAT0000456: 5'CAAAGAAUUCUCCUUUUGGGCU
Hs_miR-218_1 miScript Primer Assay	MIMAT0000275: 5'UUGUGCUUGAUCUAACCAUGU
Hs_miR-302a_2 miScript Primer Assay	MIMAT0000684: 5'UAAGUGCUUCCAUGUUUUGGUGA
Hs_miR-367_2 miScript Primer Assay	MIMAT0000719: 5'AAUUGCACUUUAGCAAUGGUGA
Hs_miR-375_2 miScript Primer Assay	MIMAT0000728: 5'UUUGUUCGUUCGGCUCGCGUGA
Hs_miR-484_1 miScript Primer Assay	MIMAT0002174: 5'UCAGGCUCAGUCCCCUCCCGAU

Table S4. Oligonucleotides and probes used in this study. Related to Experimental Procedures

SUPPLEMENTAL EXPERIMENTAL PROCEDURES

Maintenance and differentiation of human iPSCs

Generation and validation of iPSC lines is described in Lenzi et al. (Lenzi et al., 2015). All iPSC lines were maintained in Nutristem-XF (Biological Industries, Kibbutz Beit-Haemek, Israel) in plates coated with hESC-qualified Matrigel (Corning Inc., Corning, NY) and passaged every 4-5 days with 1 mg/ml Dispase (Thermo Fisher Scientific, Waltham, MA). MN differentiation protocol has been modified from Hill et al. (Hill et al., 2016). iPSCs were dissociated to single cells with Accutase (Thermo Fisher Scientific) and counted. 9×10^5 cells were seeded onto each well of a 6-well Matrigel-coated plate in Nutristem-XF supplemented with 10 µM ROCK-inhibitor (Y-27632, Sigma-Aldrich, St. Louis, MO) to enhance survival upon dissociation. The ROCK-inhibitor was withdrawn the next day. After two days (day 0), cells reached confluence and medium was switched to N2B27 Medium, composed of 50% DMEM/F12 (Sigma-Aldrich) and 50% Neurobasal (Thermo Fisher Scientific) supplemented with 1X N2 and 1X B27, 1X Glutamax, 1X MEM Non-Essential Aminoacids (all from Thermo Fisher Scientific) and 100 U/ml Penicillin + 100 µg/ml Streptomycin (Sigma Aldrich). 10 µM SB431542 (Miltenyi Biotec, Bergisch Gladbach, Germany) and 100 nM LDN-193189 (Miltenyi Biotec) were added to the medium from day 0 to 6, while 5 µM DAPT (Sigma-Aldrich) and 4 µM SU-5402 (Sigma Aldrich) were added from day 6 to 12. 1 µM all-trans Retinoic Acid (Sigma-Aldrich) and 1 µM SAG (Merck Millipore, Billerica, MA) were added to the medium from day 0 to 12. Medium was replaced daily during the course of differentiation.

Cells were dissociated at day 12 with the Papain Dissociation System (Worthington Biochemical Corp., Lakewood, NJ) and single cell suspensions were prepared for isolation in sorting buffer (PBS without Ca^{2+}/Mg^{2+}; 2.5% Horse Serum; 0.4% Glucose; DNAseI; all from Sigma-Aldrich) containing 1X B27 Supplement (Thermo Fisher Scientific).

After sorting, cells were re-plated on poly-L-ornithine (Sigma-Aldrich) and natural mouse laminin (Sigma-Aldrich) coated dishes in Neural Medium (N2B27 Medium supplemented with 20 ng/ml BDNF, 10 ng/ml GDNF, 10ng/ml CNTF, all from Peprotech, London, UK; 200 ng/ml L-ascorbic acid, Sigma-Aldrich; and ROCK-inhibitor for the first 24 hours). Neural Medium without ROCK-inhibitor was replaced every 3 days until collection of cells. The *Hb9*::GFP reporter, kindly provided by Dr. Kevin Eggan, was stably integrated in the *AAVS1* locus by targeted Zinc Finger Nucleases (ZFNs) as previously described (Wainger et al., 2014). Briefly, *AAVS1* ZFNs and the template construct containing the reporter and a puromycin resistance gene were co-transfected in iPSCs using the Neon Transfection System (Thermo Fisher Scientific) as described (Lenzi et al., 2015). After 48 hours, transfected cells were selected with 0.5 µg/ml puromycin and then clonally expanded.

Isolation of differentiated MNs by fluorescent-activated cell sorting (FACS)

Human MNs were sorted based on GFP expression from the *Hb9*::GFP reporter using a FACSAriaIII (BD Biosciences, San Jose, CA) equipped with a 488nm laser and FACSDiva software (BD Biosciences version 6.1.3). Data were analyzed using the FlowJo software (Tree Star, Ashland, OR). Briefly, cells first gated based on forward and side scatter area (FSC-A and SSC-A) plot were then detected in the green fluorescence channel for GFP expression (530/50nm filter) and collected as negative (GFP-) and positive cells (GFP+). To reduce stress for the neurons, cells were isolated in gentle conditions using a ceramic nozzle of size 100µm, a low sheath pressure of 19.84 pound-force per square inch (psi) that maintains the sample pressure at 18.96 psi and an acquisition rate of 3000 events/s. According to the different use, cells were collected in 5 and/or 15 ml polystyrene or polypropylene tubes. Following isolation, an aliquot of each tube of the sorted cells was evaluated for purity resulting in an enrichment >98-99% for each sample.

To check the course of differentiation, an aliquot of cells was acquired starting from day 6 every 2 days at the flow cytometer LSRFortessa (BD Biosciences), equipped with a 488nm laser, to evaluate GFP expression levels.

Real-time qRT-PCR and western blot analysis

Total RNA was extracted with the Quick RNA MiniPrep (Zymo Research, Irvine, CA) and retrotranscribed with SuperScript VILO (Thermo Fisher Scientific) or miScript II RT (Qiagen, Venlo, Netherlands). Real-time qRT-PCR analysis was performed with SYBR Green Power-UP (Thermo Fisher Scientific) or SYBR Green PCR Master Mix (Qiagen) in a ViiA7 Real Time PCR System (Thermo Fisher Scientific) and calculations performed with the delta delta Ct method. The internal control for mRNA analysis is the housekeeping gene *ATP5O* (ATP synthase, H+ transporting, mitochondrial F1 complex, O subunit). For miRNA analysis internal control is U25 (SNORD_25). Primers sequences are reported in Table S4.

Western blot analysis of p53 protein levels was carried out with NuPAGE 4-12% Bis-Tris gels (Thermo Fisher Scientific) in MOPS-SDS buffer, using anti-p53 (fl-393; Santa Cruz, Dallas, TX) and, as a loading control, anti-GAPDH (sc-32233; Santa Cruz) antibodies. Images were acquired with the Chemidoc MP (BioRad, Hercules, CA).

miRNAs 384 array

200ng total RNA from MNs was retrotranscribed using the TaqMan MicroRNA RT Kit (Thermo Fisher Scientific). The real-time detection of the miRNA levels was performed using the TaqMan® Human MicroRNA Array A (Thermo Fisher Scientific), according to manufacturer's instructions, in a ViiA7 Real Time PCR System (Thermo Fisher Scientific). The values obtained were normalized for snoRNA-U44.

RNA sequencing and bioinformatics analysis

Total RNA was extracted from iPSC-derived MNs (GFP-negative and positive with a FUS^{WT} genotype, day12; FUS^{WT} and FUS^{P525L}, day 12+7) and sequenced on a Illumina Hiseq 2500 Sequencing system using TruSeq Stranded Total RNA Library Prep Kit with Ribo-Zero treatment (Illumina, San Diego, CA) at the Institute of Applied Genomics (IGA; Udine, Italy). An average of about 21 million 125 base pairs long paired-end reads were produced for each sample.

RNA-Seq reads were initially trimmed using the Trimmomatic software (Bolger et al., 2014) to remove adapter sequences and poor quality bases; the minimum read length after trimming was set to 18. After that, Bowtie 2 (Langmead and Salzberg, 2012) was used to align reads to human rRNA sequences; reads mapping to these sequences were filtered out. In order to calculate the distribution of the inner distance between mate pairs, reads were aligned to a non-redundant set of human RNA sequences derived from Ensembl 77 gene annotation (Flicek et al., 2014) using BWA software (H. Li and Durbin, 2010); this mapper was chosen because of its ability to automatically infer the insert size. Mean and variance of inner distance distribution were estimated from aligned read pairs whose inner distance was within interval [Q1-2(Q3-Q1),Q3+2(Q3-Q1)] (Q1=first quartile, Q3=third quartile), the same as used by BWA to estimate the insert size. TopHat2 (Kim et al., 2013) was employed to align reads to GRCh38 human genome and Ensembl transcriptome using parameters *-i 50 -r -32 --mate-std-dev 58 --library-type fr-firststrand*. Read counts for Ensembl 77 human genes were calculated using htseq-count software (Anders et al., 2015), specifying the *intersection-strict* option. Number of reads and mapping statistics are reported in Table S1. edgeR software (Robinson et al., 2010) was used to find differentially expressed genes in GFP-positive vs GFP-negative and FUS^{WT} vs FUS^{P525L} comparisons. In both cases, TMM normalization was applied to read counts after filtering genes with a CPM (Count Per Million) value less than 1 in at least three (in GFP-positive vs GFP-negative comparison) or four (in FUS^{WT} vs FUS^{P525L} comparisons) samples. MDS plots and Pearson correlation-based sample correlation matrices were drawn based on log2-transformed normalized read counts. For FUS^{WT} vs FUS^{P525L} comparison, samples originating from the same differentiation experiment showed some degree of pairing and this was taken into account when performing differential expression analysis. An additive model was fitted to adjust for baseline differences between the three independent differentiation experiments: design <- model.matrix (~ experiment + condition). Model fitting and testing was performed using *glmFIT* and *glmLRT* functions. Heatmaps of differentially expressed genes were plotted based on mean-centered log2-transformed RPKM values, calculated using *rpkm* function.

Functional enrichment analysis of genes deregulated upon FUS mutation was performed by providing the list of differentially expressed protein-coding genes to FIDEA Web Server (D'Andrea et al., 2013), using the list of protein-coding genes that passed the CPM-based filter as background. GSEA analysis was performed using GSEA software (Hill et al., 2016; Subramanian et al., 2005), with the *permutation type* parameter set to *gene set*.

Cufflinks software (Trapnell et al., 2010) was employed to evaluate transcript-level expression in FUS^{WT} and FUS^{P525L} conditions, using parameters *--compatible-hits-norm --max-frag-multihits 1*. Transcripts with FPKM > 0.1 and belonging to genes with FPKM > 0.5 in at least three samples were flagged as expressed.

CLIP-Seq data reanalysis

Raw reads from FUS HITS-CLIP experiment conducted by Lagier-Tourenne and coworkers (Lagier-Tourenne et al., 2012) on human brain cortex were downloaded from GEO. First, adapter and quality trimming of reads was performed using Trimmomatic; Cutadapt was then used to remove all the adapter sequences that were not trimmed in the first phase. Trimmed reads were aligned to GRCh38 using Bowtie (Langmead et al., 2009) with parameters *-a -m 1 --best --strata*. Duplicate reads, which could represent PCR artifacts, were removed using MarkDuplicates from Picard (picard.sourceforge.net/command-line-overview.shtml). Tools from the Pyicoteo suite (Althammer et al., 2011) were used to call CLIP-Seq peaks. First, all reads were extended to a length of 36 nucleotides using the pyicos extend tool. Then, CLIP-Seq peak calling was performed using the pyicoclip tool. Ensembl 77 GTF file was supplied to generate exploratory regions, using the option *--region-magic genebody*. Only peaks with p-value < 0.001 were retained. Colocalization of FUS CLIP-Seq peaks with different regions of expressed protein-coding transcripts was evaluated as follows: each protein-coding locus was divided into coding sequence (CDS), 5' UTR, 3'UTR, proximal and distal intron regions (the latter being defined as the intronic regions which are more than 500 bp far from the nearest exon-intron boundary), giving priority to CDS over the other regions; then each peak was assigned a region based on the position of the peak summit using the BEDTools software suite (http://bedtools.readthedocs.io/). Enrichment of peaks in each region relative to region size was computed as described (Kapeli et al., 2016). For the analysis of differential FUS binding between deregulated and non-deregulated genes, bound genes were defined as those hosting at least one FUS CLIP-Seq peak, either within the entire gene body or in a specific pre-mRNA region.

TDP-43 binding sites obtained by iCLIP in human brain (Tollervey et al., 2011) were downloaded from starBase v2.0 Web Server (J.-H. Li et al., 2014). hg19 coordinates were converted to GRCh38 coordinates using the liftOver tool (The UCSC Genome Browser Database: update 2006). The center of each iCLIP cluster was used to assign it to a pre-mRNA region.

Small RNA-Seq

Total RNA was extracted from iPSC-derived MNs (FUS^{WT} and FUS^{P525L}, day 12+7) and sequenced on a Illumina Hiseq 2500 Sequencing system using TruSeq Small RNA Library (Illumina) at the Institute of Applied Genomics (IGA; Udine, Italy). An average of about 17 million 50 base pairs long single-end reads were produced for each sample. mirPRo software (Shi et al., 2015; Subramanian et al., 2005) was used to remove adapter sequences, map reads to human pre-miRNA sequences downloaded from mirBase v21 (Kozomara and Griffiths-Jones, 2014) using NovoAlign (H. Li and Homer, 2010), and calculate read counts for mature miRNAs. Number of reads and mapping statistics are reported in Table S1. Starting from the raw counts, sample clustering and differential expression of mature miRNAs were performed using the same procedure adopted for FUS^{WT} vs FUS^{P525L} comparison. Samples originating from the same differentiation batch were mildly correlated, so we opted for a paired design when performing differential expression analysis. The heatmap of deregulated mature miRNAs was plotted based on mean-centered log2-transformed CPM values.

Immunostaining

MNs were re-plated on matrigel-coated dishes and cultured for additional 3 days (day12+3), then were fixed in 2% paraformaldehyde for 15 minutes at room temperature and washed twice with PBS. Fixed cells were then permeabilized with PBS containing 1% BSA and 0.2% Triton X-100 and incubated 1h with primary antibody anti-Islet-1/2 (1:50, 39.4D5 DSHB, Iowa City, Iowa) and TUJ1 (1:200; T2200; Sigma-Aldrich) at room temperature. The secondary antibodies are goat anti-mouse Alexa Fluor 488 (1:250, Thermo Fisher Scientific) and goat anti-rabbit Cy3 (1:250, Jackson ImmunoResearch, Suffolk, UK). DAPI (Sigma-Aldrich) was used to stain nuclei. Fluorescent images were acquired using a 20X LWD objective mounted on an inverted iX73 microscope (both Olympus, Tokyo, Japan) with Lumencor Spectra X LED illumination, a CoolSNAP MYO CCD camera (Photometrics, Tucson, AZ), and MetaMorph software (Molecular Devices, Sunnyvale, CA).

iPSCs were fixed in 4% paraformaldehyde for 15 minutes at room temperature and washed twice with PBS. Fixed cells were then permeabilized with PBS containing 1% BSA and 0.2% Triton X-100 and incubated with the primary antibody anti-FUS/TLS (4H11) (1:100; SC-47711; Santa Cruz Biotechnologies) for 1 hour at room temperature. The secondary antibody is goat anti-mouse Alexa Fluor 488 (1:250, Thermo Fisher Scientific). DAPI (Sigma-Aldrich) was used to stain nuclei. Confocal images were acquired at the Olympus iX83 FluoView1200 laser scanning confocal microscope using a UPLSAPO60xO, NA 1,35 oil objective. The standard setting for DAPI and Alexa Fluor 488 emission and 405nm and 473nm laser for excitation were used. Images were acquired at 800x800 pixel, 4x zoom, line scan sequential mode.

FUS knockdown

For FUS knockdown experiments, FUS^{WT} iPSCs were induced to differentiate and transfected at 8 and 10 days with 40 nM anti-FUS siRNAs (Hs_FUS_4 FlexiTube siRNA, SI00070518, Qiagen) or scramble control siRNAs (AllStars Neg. Control 414 siRNA, 1027281, Qiagen) using Lipofectamine RNAi-Max (Thermo Fisher Scientific), according to manufacturer's instructions.

miRNA mimics transfection

FUS^{P525L} iPSCs were induced to differentiate into MNs for 14 days. After dissociation with Accutase (Thermo Fisher Scientific), cells were seeded on Matrigel-coated plates and then transfected after 48 hours with 10nM mirVana miRNA mimics (Thermo Fisher Scientific) (microRNA-375-3p MIMAT0000728; miRNA Mimic Negative Control#1 Cat. 4464058) using Lipofectamine 2000 (Thermo Fisher Scientific), according to manufacturer's instructions. RNA was collected for real-time qRT-PCR analysis after 48 hours.

SUPPLEMENTAL REFERENCES

Althammer, S., González-Vallinas, J., Ballaré, C., Beato, M., Eyras, E., 2011. Pyicos: a versatile toolkit for the analysis of high-throughput sequencing data. Bioinformatics 27, 3333–3340. doi:10.1093/bioinformatics/btr570

Anders, S., Pyl, P. T., Huber, W., 2015. HTSeq--a Python framework to work with high-throughput sequencing data. Bioinformatics 31, 166–169. doi:10.1093/bioinformatics/btu638

Bolger, A.M., Lohse, M., Usadel, B., 2014. Trimmomatic: a flexible trimmer for Illumina sequence data. Bioinformatics 30, 2114–2120. doi:10.1093/bioinformatics/btu170

D'Andrea, D., Grassi, L., Mazzapioda, M., Tramontano, A., 2013. FIDEA: a server for the functional interpretation of differential expression analysis. Nucleic Acids Res 41, W84–8. doi:10.1093/nar/gkt516

Flicek, P., Amode, M.R., Barrell, D., Beal, K., Billis, K., Brent, S., Carvalho-Silva, D., Clapham, P., Coates, G., Fitzgerald, S., Gil, L., Girón, C.G., Gordon, L., Hourlier, T., Hunt, S., Johnson, N., Juettemann, T., Kähäri, A.K., Keenan, S., Kulesha, E., Martin, F.J., Maurel, T., McLaren, W.M., Murphy, D.N., Nag, R., Overduin, B., Pignatelli, M., Pritchard, B., Pritchard, E., Riat, H.S., Ruffier, M., Sheppard, D., Taylor, K., Thormann, A., Trevanion, S.J., Vullo, A., Wilder, S.P., Wilson, M., Zadissa, A., Aken, B.L., Birney, E., Cunningham, F., Harrow, J., Herrero, J., Hubbard, T.J.P., Kinsella, R., Muffato, M., Parker, A., Spudich, G., Yates, A., Zerbino, D.R., Searle, S.M.J., 2014. Ensembl 2014. Nucleic Acids Res 42, D749–55. doi:10.1093/nar/gkt1196

Hill, S.J., Mordes, D.A., Cameron, L.A., Neuberg, D.S., Landini, S., Eggan, K., Livingston, D.M., 2016. Two familial ALS proteins function in prevention/repair of transcription-associated DNA damage. Proc Natl Acad Sci USA 113, E7701–E7709. doi:10.1073/pnas.1611673113

Kapeli, K., Pratt, G.A., Vu, A.Q., Hutt, K.R., Martinez, F.J., Sundararaman, B., Batra, R., Freese, P., Lambert, N.J., Huelga, S.C., Chun, S.J., Liang, T.Y., Chang, J., Donohue, J.P., Shiue, L., Zhang, J., Zhu, H., Cambi, F., Kasarskis, E., Hoon, S., Ares, M., Burge, C.B., Ravits, J., Rigo, F., Yeo, G.W., 2016. Distinct and shared functions of ALS-associated proteins TDP-43, FUS and TAF15 revealed by multisystem analyses. Nat Commun 7, 12143. doi:10.1038/ncomms12143

Kim, D., Pertea, G., Trapnell, C., Pimentel, H., Kelley, R., Salzberg, S.L., 2013. TopHat2: accurate alignment of transcriptomes in the presence of insertions, deletions and gene fusions. Genome Biol. 14, R36. doi:10.1186/gb-2013-14-4-r36

Kozomara, A., Griffiths-Jones, S., 2014. miRBase: annotating high confidence microRNAs using deep sequencing data. Nucleic Acids Res 42, D68–73. doi:10.1093/nar/gkt1181

Lagier-Tourenne, C., Polymenidou, M., Hutt, K.R., Vu, A.Q., Baughn, M., Huelga, S.C., Clutario, K.M., Ling, S.-C., Liang, T.Y., Mazur, C., Wancewicz, E., Kim, A.S., Watt, A., Freier, S., Hicks, G.G., Donohue, J.P., Shiue, L., Bennett, C.F., Ravits, J., Cleveland, D.W., Yeo, G.W., 2012. Divergent roles of ALS-linked proteins FUS/TLS and TDP-43 intersect in processing long pre-mRNAs. Nat Neurosci. doi:10.1038/nn.3230

Langmead, B., Salzberg, S.L., 2012. Fast gapped-read alignment with Bowtie 2. Nat Methods 9, 357–359. doi:10.1038/nmeth.1923

Langmead, B., Trapnell, C., Pop, M., Salzberg, S.L., 2009. Ultrafast and memory-efficient alignment of short DNA sequences to the human genome. Genome Biol. 10, R25. doi:10.1186/gb-2009-10-3-r25

Lenzi, J., De Santis, R., de Turris, V., Morlando, M., Laneve, P., Calvo, A., Caliendo, V., Chiò, A., Rosa, A., Bozzoni, I., 2015. ALS mutant FUS proteins are recruited into stress granules in induced Pluripotent Stem Cells (iPSCs) derived motoneurons. Dis Model Mech 8, 755–766. doi:10.1242/dmm.020099

Li, H., Durbin, R., 2010. Fast and accurate long-read alignment with Burrows-Wheeler transform. Bioinformatics 26, 589–595. doi:10.1093/bioinformatics/btp698

Li, H., Homer, N., 2010. A survey of sequence alignment algorithms for next-generation sequencing. Brief. Bioinformatics 11, 473–483. doi:10.1093/bib/bbq015

Li, J.-H., Liu, S., Zhou, H., Qu, L.-H., Yang, J.-H., 2014. starBase v2.0: decoding miRNA-ceRNA, miRNA-ncRNA and protein-RNA interaction networks from large-scale CLIP-Seq data. Nucleic Acids Res 42, D92–7. doi:10.1093/nar/gkt1248

Robinson, M.D., McCarthy, D.J., Smyth, G.K., 2010. edgeR: a Bioconductor package for differential expression analysis of digital gene expression data. Bioinformatics 26, 139–140. doi:10.1093/bioinformatics/btp616

Shi, J., Dong, M., Li, L., Liu, L., Luz-Madrigal, A., Tsonis, P.A., Del Rio-Tsonis, K., Liang, C., 2015. mirPRo-a novel standalone program for differential expression and variation analysis of miRNAs. Sci Rep 5, 14617. doi:10.1038/srep14617

Subramanian, A., Tamayo, P., Mootha, V.K., Mukherjee, S., Ebert, B.L., Gillette, M.A., Paulovich, A., Pomeroy, S.L., Golub, T.R., Lander, E.S., Mesirov, J.P., 2005. Gene set enrichment analysis: a knowledge-based approach for interpreting genome-wide expression profiles. Proc Natl Acad Sci USA 102, 15545–15550. doi:10.1073/pnas.0506580102

Tollervey, J.R., Curk, T., Rogelj, B., Briese, M., Cereda, M., Kayikci, M., König, J., Hortobágyi, T., Nishimura, A.L., Župunski, V., Patani, R., Chandran, S., Rot, G., Zupan, B., Shaw, C.E., Ule, J., 2011. Characterizing the RNA targets and position-dependent splicing regulation by TDP-43. Nature Publishing Group 14, 452–458. doi:10.1038/nn.2778

Trapnell, C., Williams, B.A., Pertea, G., Mortazavi, A., Kwan, G., van Baren, M.J., Salzberg, S.L., Wold, B.J., Pachter, L., 2010. Transcript assembly and quantification by RNA-Seq reveals unannotated transcripts and isoform switching during cell differentiation. Nat Biotechnol 28, 511–515. doi:10.1038/nbt.1621

Wainger, B.J., Kiskinis, E., Mellin, C., Wiskow, O., Han, S.S.W., Sandoe, J., Perez, N.P., Williams, L.A., Lee, S., Boulting, G., Berry, J.D., Brown, R.H., Cudkowicz, M.E., Bean, B.P., Eggan, K., Woolf, C.J., 2014. Intrinsic membrane hyperexcitability of amyotrophic lateral sclerosis patient-derived motor neurons. Cell Rep 7, 1–11. doi:10.1016/j.celrep.2014.03.019